Ore Geology Reviews 144 (2022) 104816

Contents lists available at ScienceDirect

Ore Geology Reviews

journal homepage: www.elsevier.com/locate/oregeorev

Two hydrothermal events associated with Au mineralization in the Youjiang Basin, southwestern China

Lujing Zheng [a,b], Qinping Tan [c,*], Yujun Zuo [a,*], Yong Xia [c], Zhuojun Xie [c], Lulin Zheng [a], Jianzhong Liu [d,e]

[a] College of Mining, Guizhou University, Guiyang 550025, China
[b] Guizhou Jinfeng Mining Limited, Southwest of Guizhou, Guizhou, Guiyang 550025, China
[c] State Key Laboratory of Ore Deposit Geochemistry, Institute of Geochemistry, Chinese Academy of Sciences, Guiyang 550081, China
[d] Technology Innovation Center of Mineral Resources Explorations in Bedrock Zones, Ministry of Natural Resources of People's Republic of China, Guiyang 550081, China
[e] Guizhou Bureau of Geology and Mineral Exploration & Development, Guiyang 550018, China

ARTICLE INFO

Keywords:
Mineralization
Carlin-type Au deposit
Lannigou
Youjiang Basin

ABSTRACT

The Youjiang Basin in southwestern China hosts remarkably large amounts of Carlin-type Au deposits. In such deposits, Au is mainly ionically bound to arsenian pyrite characterized by core and rim textures. Understanding the formation mechanism of zoned pyrite may improve our understanding of the genesis of massive Carlin-type Au deposits. This study examined the elemental content, mineral composition, and pyrite texture and chemistry of wall rock and ore from the Lannigou Au deposit, one of the largest Carlin-type Au deposits in the Youjiang Basin, to identify the genetic mechanisms of zoned pyrite.

Five distinct types of pyrites, i.e., pyrite 1 (Py1), 2 (Py2), 3 (Py3), 4 (Py4), and ore pyrite (OPy), were identified in the Lannigou Au deposit. Py1, Py2, and Py3 were mainly observed in the wall rock, whereas Py4 and OPy, constituting the core and rim of zoned pyrite, respectively, were only discovered in the ore. Mineral mapping of the wall rock and ore indicated that pyrite is scarce in the wall rock (0.021 vol%). However, the amount of zoned pyrite significantly increased in the ore (1.275 vol%). Py1, Py2, and Py3, showing framboidal, nodular, and fine euhedral microcrystal textures, had high Pb, Co, Ni, Mn, Zn, and Mo contents (medians ranging from 10 to 1,000 ppm) and variable $\delta^{34}S$ compositions ranging from −5.1 to 35.4‰, implying a sedimentary (syngenetic or diagenetic) origin. Py4 was homogeneous and contained numerous illite and quartz inclusions and fractures. In contrast, OPy showed multiple As-rich sub-bands and a lack of illite or quartz inclusions and fractures. Py4 had significantly lower Au, As, Tl, and Cu contents than OPy; however, Py4 had Pb, Co, Ni, Mn, Zn, and Mo contents similar to OPy. The range of $\delta^{34}S$ values for Py4 and OPy were both narrow, but Py4 (7.6 to 13.3‰, with an average of 9.1‰) had lower $\delta^{34}S$ values than OPy (9.4–14.1‰, with an average of 12.4‰). These texture and chemical features indicate that Py4 likely sedimented from a pre-ore hydrothermal fluid, but not at the early stage of the ore-forming fluid.

Hydrothermal pyrite cores were also widespread and exhibited textural and chemical differences compared to Au-rich pyrite rims from other Au deposits in the Youjiang Basin. Based on the two geochronological clusters of Au deposits in the Youjiang Basin, we inferred the occurrence of at least two episodes of large-scale hydrothermal events. The two hydrothermal fluid episodes, which contributed to the zoned pyrite formation, likely originated from the mixing of initial magmatic fluid with $\delta^{34}S$ values of $\sim 0 \pm 5$‰ and basin brine with elevated $\delta^{34}S$ values ($\delta^{34}S > 18$‰). Pre-ore hydrothermal pyrite likely resulted in the rapid non-equilibrium crystallization of ore pyrite; thus, more Carlin-suite elements were captured by ore pyrite. Additionally, low-grade Au orebodies may have locally formed during the pre-ore hydrothermal event. These multiple hydrothermal events may have been crucial for the formation of massive Carlin-type Au deposits in the Youjiang Basin.

* Corresponding authors.
E-mail addresses: tanqinping@mail.gyig.ac.cn (Q. Tan), zuo_yujun@163.com (Y. Zuo).

https://doi.org/10.1016/j.oregeorev.2022.104816
Received 6 January 2022; Received in revised form 25 February 2022; Accepted 4 March 2022
Available online 7 March 2022

1. Introduction

Carlin-type deposits account for approximately 8 % of the annual worldwide Au production (Frimmel, 2008) and are primarily concentrated in north-central Nevada, USA, and the Youjiang Basin in southwestern China (Muntean and Cline, 2018). Nevada Carlin-type deposits constitute the world's second-largest amount of Au (~7,930 tons), after deposits in South Africa (Muntean et al., 2011). Carlin-type deposits in the Youjiang Basin have an Au endowment of >900 tons (Liu et al., 2020)—it is the second-largest Carlin-type Au deposit district worldwide.

Carlin-type Au deposits in the USA and China share many common features, such as carbonate host rocks, hydrothermal alterations, geochemical signatures, "invisible" Au in arsenian pyrite, and mineral paragenesis (Cline et al., 2005; Su et al., 2009a; Cline et al., 2013; Xie et al., 2018a). Particularly, zoned arsenian pyrite, commonly consisting of barren pyrite cores and Au-bearing pyrite rims, is one of the most remarkable characteristics of Carlin-type Au deposits. Sulfidation of H_2S-rich and Fe-poor fluids reacting with Fe-bearing minerals in host rocks is an important precipitation mechanism for ore pyrite (Hofstra and Cline, 2000; Cline et al., 2005; Su et al., 2009a). *In situ* analytical methods, such as laser ablation inductively coupled plasma mass spectrometry (LA-ICP-MS), LA multi-collector (MC) ICP-MS, sensitive high-resolution ion microprobe (SHRIMP), and secondary ion mass spectrometry (SIMS), have been widely used for S and trace element composition measurements of zoned pyrite from Carlin-type Au deposits (e.g., Kesler et al., 2005; Barker et al., 2009; Hou et al., 2016; Xie et al., 2018b; Yan et al., 2018; Li et al., 2019; Liang et al., 2020; He et al., 2021; Lin et al., 2021). *In situ* LA-ICP-MS analysis and SIMS mapping have revealed fluctuations in the elemental and isotope compositions of pyrite rims, implying that the ore-forming fluid periodically intruded into the hydrothermal systems (e.g., Barker et al., 2009; Yan et al., 2018; Li et al., 2020; Liang et al., 2020; Zhao et al., 2020). Based on the *in situ* S isotope compositions of pyrite rims, three groups of genetic models have been proposed for Carlin-type gold deposits, including magmatic (Cline et al., 2005; Ressel and Henry, 2006; Muntean et al., 2011; Hou et al., 2016; Xie et al., 2018b), metamorphic (Groves et al., 1998; Hofstra and Cline, 2000; Su et al., 2009a; 2018; Li et al., 2020; Lin et al., 2021), and circulated meteoric water or basin brines (Ilchik and Barton, 1997; Hu et al., 2002; Emsbo et al., 2003; Gu et al., 2012).

Most studies to date have mainly focused on Au-rich pyrite rims, whereas studies on pyrite cores are scarce. Partial pyrite cores in high-grade ores from the Getchell and Cortez Hills Carlin-type Au deposits in Nevada show elevated Hg, Tl, Cu, W, Pb, Sn, and Bi concentrations (Clark Maroun et al., 2017; Xie et al., 2018a), which is consistent with a hydrothermal origin. Clark Maroun et al. (2017) suggested that pyrite cores could have formed during a magmatic event before or early on during the Carlin event as Sn and Pb are not constituents of Carlin-suite metal; low-temperature Carlin fluids unlikely transport Sn. Owing to a lack of evidence on pre-ore hydrothermal events or magmatic activity in the vicinity of Au deposits in the Youjiang Basin, most studies ascribed pyrite cores in ore to a sedimentary (syngenetic or diagenetic) origin with a porous texture and low As and Au contents (Su et al., 2012; Hou et al., 2016; Xie et al., 2018b; Yan et al., 2018; Li et al., 2019; 2020; Wei et al., 2020; He et al., 2021), whereas others have proposed that pyrite cores formed during the early ore stage owing to a similar S isotope composition as that of pyrite rims (Liang et al., 2020; Zhao et al., 2020; Lin et al., 2021). The host rocks (e.g., impure silty limestone or calcareous mudstone and siltstone) of the Carlin-type Au deposits usually lack sulfide minerals. Ubiquitous pyrite cores in the Carlin-type Au deposits may have not only formed via sedimentation or diagenesis, but also because of other geological events. Pyrite cores in ore may have played an important role in the formation of massive Carlin-type Au deposits. Therefore, a systematic comparative study of pyrite cores, ore pyrite, and sedimentary pyrite is essential for uncovering the genetic mechanism of pyrite cores in Carlin-type Au deposits.

In this study, the Lannigou Au deposit, one of the largest Au deposits in the Youjiang Basin, was selected as a case study. Wall rock and ore samples were collected from a drill core along a short transect across a high-grade Au fault zone. Mineral mapping of the polished wall rock and ore samples was obtained by the TESCAN integrated mineral analyzer system (TIMA). High-resolution scanning electron microscope (SEM), LA-ICP-MS, and LA-MC-ICP-MS analyses were performed to reveal the texture and chemical characteristics of pyrite in the wall rock and ore. Published *in situ* elemental and S isotope data on zoned pyrite from other Au deposits in the Youjiang Basin were also compiled. Pyrite in unaltered wall rock is rare, whereas the presence of zoned pyrite significantly increases in ore. Pyrite cores in the ore, commonly containing fractures filled by ore-stage pyrite, exhibit textural and chemical affinities of typical hydrothermal pyrite, likely implying large-scale pre-ore hydrothermal activity in the Youjiang Basin.

2. Regional geology

The Youjiang Basin is located at the junction of Guizhou, Guangxi, and Yunnan in southwestern China (Fig. 1) and is commonly referred to as the "Dian-Qian-Gui" Golden Triangle Region (Chen et al., 2015). It is bound to the northeast and northwest by the Ziyun-Yadu and Mile-Shizong faults, respectively, separating the basin from the Yangtze craton (Hou et al., 2016; Tan et al., 2019). The southeastern and southwestern edges of the basin are separated from the Cathaysia and Simao blocks by the Pingxiang-Nanning and Red River faults, respectively (Hou et al., 2016; Su et al., 2018).

Devonian rifting opened up the Youjiang Basin at the southwestern margin of the Precambrian Yangtze craton (Su et al., 2018), which then experienced a rifting stage from the late Early Devonian to the Late Devonian, followed by passive continental margin settings from the Early Carboniferous to the Early Triassic and a foreland basin setting during the Middle Triassic (Du et al., 2013). Following tectonic evolution, a sequence of deep-water basin-facies sedimentary rocks dominated by siltstone and siliceous rocks, interbedded with thinly layered carbonate rock and sandstone, were deposited in the southeastern region of the basin (Xie et al., 2018a). In the northwestern region of the basin, a sequence of shallow-water platform-facies sedimentary rocks, consisting of carbonates interbedded with calcareous siltstone and sandstone, and Permian Emeishan flood basalts were formed (Su et al., 2018). These sedimentary rocks host most of the Au deposits in the Youjiang Basin.

Tectonically, the Youjiang Basin is in the hinge area of the Tethyan and Pacific tectonic domains, such that the basin has been deformed by two subduction-related tectonic events (Pi et al., 2017; Chen et al., 2019; Tan et al., 2019; Gao et al., 2021; Jin et al., 2021). Continued subduction of the Paleo-Tethys Ocean beneath the Indochina Block eventually led to the Indochina-South China collision during the Middle to Late Triassic (Lai et al., 2014; Zaw et al., 2014). This collision resulted in a sequence of parallel NW-striking faults and folds in the Youjiang Basin. Alternatively, a flat-slab subduction of the Paleo-Pacific plate beneath South China began approximately 250 Ma ago; by the Late Triassic (approximately 210 Ma), the orogenic front had propagated > 1,000 km away from the hypothesized trench (Li and Li, 2007), causing NE-striking faulting and folding of the sequences in the Youjiang Basin. The younger magmatic ages toward the coast after 150 Ma have been interpreted as slab rollback, corresponding to a tectonic transition from contraction to large-scale extension (Li and Li, 2007). The Au deposits in the Youjiang Basin may have formed at the post-collisional extensional dynamic setting of these subduction events (Pi et al., 2017; Su et al., 2018; Chen et al., 2019; Tan et al., 2019; Gao et al., 2021; Jin et al., 2021), which is analogous to that of Eocene Carlin-type Au deposits in Nevada (Cline et al., 2005; Ressel and Henry, 2006; Muntean et al., 2011).

Igneous rocks in the Youjiang Basin are scarce and mainly consist of Permian Emeishan flood basalts in the northwest, diabase intrusions in

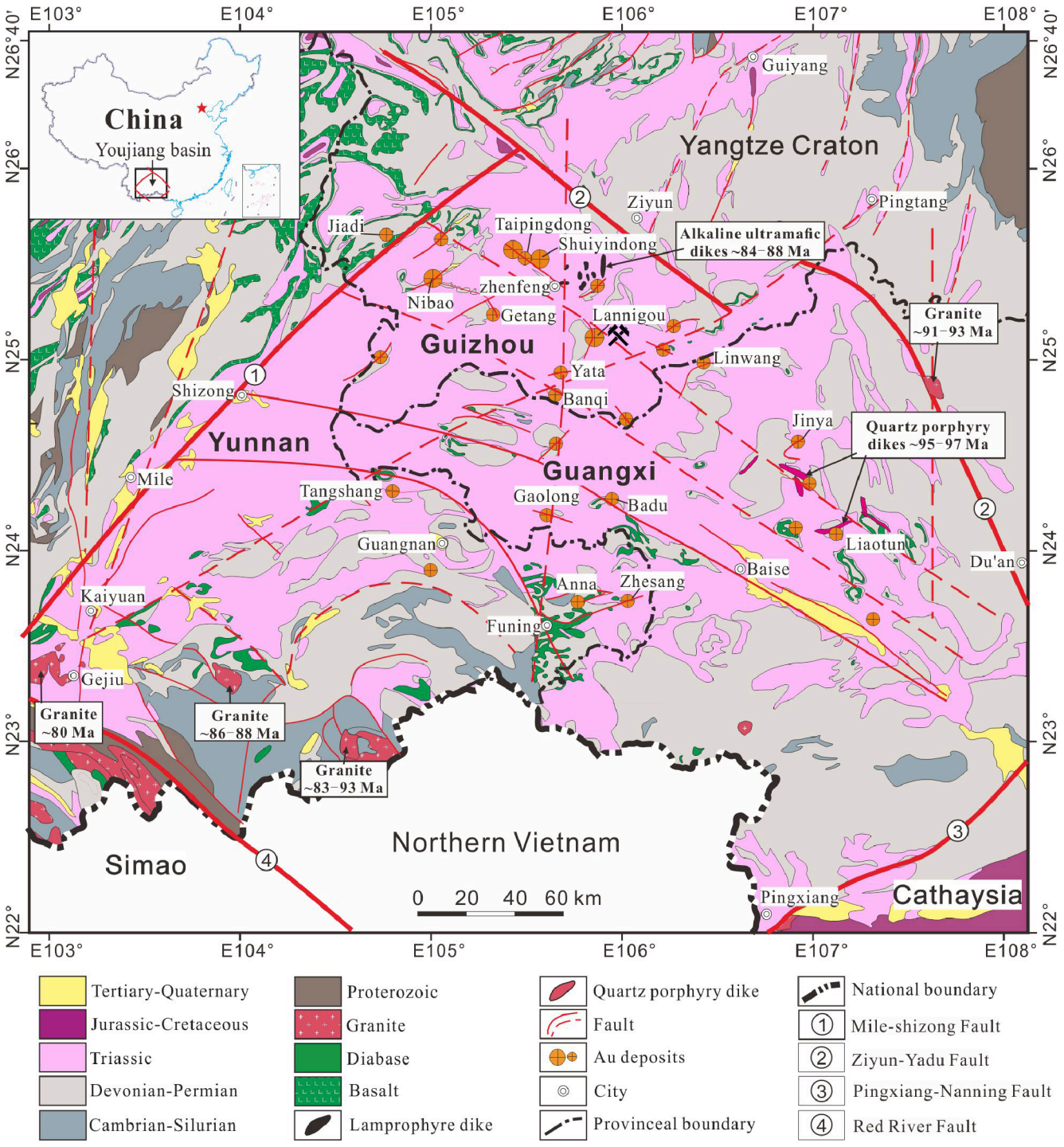

Fig. 1. Regional geological map of the Youjiang Basin, southwestern China, showing the distributions of exposed strata, igneous rocks, basement-penetrating faults, and Carlin-type Au deposits [modified from Su et al. (2018) and Tan et al. (2019)].

the south, and granite plutons in the southwest and eastern regions of the basin (Fig. 1). Two periods of diabase intrusion have been identified based on cross-cutting relationships, petrogeochemistry, and geochronology (Pi et al., 2016; Jiang et al., 2017). Early intrusions are widespread in the southern parts of the basin and are part of the Emeishan large igneous province that formed at 260 Ma (Zhou et al., 2006). Late intrusions (ca. 212–215 Ma), exposed mainly in the Funing area of Yunnan Province, resulted from the post-collision of the Indochina Block with the South China Block (Pi et al., 2016; Gao et al., 2021). In the southwestern and eastern parts of the basin, granite plutons (ca. 80–100 Ma; Fig. 1) have been interpreted to have mainly derived from crustal melts with minor mantle input during lithospheric extension of the South China Block in the late Mesozoic (Cai et al., 2006; Liu et al., 2007; Cheng and Mao, 2010; Cheng et al., 2010; Zhao et al., 2018). Some of the granitic intrusions contributed to the formation of polymetallic W-Sn deposits (Mao et al., 2013). Additionally, sparse alkali ultramafic dikes (ca. 84–88 Ma; Chen et al., 2009; Liu et al., 2010) and quartz porphyry dikes (ca. 95–97 Ma; Chen et al., 2012; Zhu et al., 2017) are exposed in the northeastern part of the basin. These dikes are contemporaneous with the granite plutons in the southwestern and eastern parts of the

basin, implying that they may have formed in a similar lithospheric extension setting (Zhu et al., 2017).

3. Geology of the Lannigou Au deposit

Lannigou, also known as Jinfeng, is the second-largest Carlin-type gold deposit in the Youjiang Basin after the Shuiyindong deposit. At the end of 2016, there was a proven Au endowment of 109 tons in the open-pit and underground mines, with an average grade of 3.83 g/t (Su et al., 2018). The geological features of the Lannigou deposit have been comprehensively described by Zhang et al. (2003), Ilchik et al. (2005), Chen et al. (2011), Su et al. (2018), and Xie et al. (2018a). Fig. 2 shows the main characteristics of the deposit, which are briefly summarized below.

Lannigou lies on the northeastern limb of the NNE-trending Laizhishan anticline. There are two different stratigraphic units that occur in the Lannigou mining area (Fig. 2). The western part is a Permian platform of massive shallow-marine carbonate rocks, mainly composed of the Lower Permian Qixia and Maokou formations, the Upper Permian Wujiaping Formation, and the Middle to Late Permian reef limestone. The stratigraphic units in the eastern part are primarily composed of the Middle Triassic Xuman, Niluo, and Bianyang formations, which consist of terrigenous detrital deep-marine facies sediments. The Bianyang and Xuman formations yield most of the ore-bearing stratigraphic units, where the former is dominant in shallow profiles of the deposit. The Bianyang Formation, with a thickness of >400 m, comprises moderately bedded calcareous arenite and siltstone interbedded with thin-layered calcareous mudstone. The Xuman Formation, with a thickness of >250 m, consists of thick-bedded to massive calcareous mudstone and siltstone with several interlayered sandstone lenses.

The sedimentary sequences in the Lannigou mining area were strongly folded and cut by a series of NW- or NS-striking thrust faults (e.g., F3, F5, and F7). These faults were cut by a series of younger NE-striking steep faults (e.g., F2 and F12). NE-SW compression produced a complex series of tight to gentle folds and thrust faults, interpreted to have hosted fluid flow (Ilchik et al., 2005). The major orebodies commonly occur as veins and lenses with quartz-calcite veins and disseminated pyrite in the steeply-dipping NW-striking faults (e.g., F3 and F6) and at the intersection of the NW- and NE-striking faults (e.g., F3 and F2) (Su et al., 2018; Yan et al., 2018). A fractured zone along the NW-striking F3 fault hosts the largest orebody. The average thickness of this orebody is approximately 8 m, with a vertical continuity of >1,000 m, which remains open to the SE (Chen et al., 2011).

Wall rock alterations and mineral paragenesis identified at Lannigou resemble those of other Carlin-type deposits in the USA and China (Cline et al., 2013; Xie et al., 2018b). Similarities include the dissolution and silicification of carbonate; argillization of silicates; sulfidation of Fe in the rock, forming Au-bearing arsenian pyrite; and late open-space deposition of stibnite, realgar, orpiment, cinnabar, quartz, dolomite, and calcite (Fig. 3). Arsenian pyrite is the principal ore mineral that hosts "invisible" ionic Au (Liang et al., 2021). Late-stage gangue minerals include quartz, calcite, and dolomite, which commonly fill fractures at the periphery of high-grade ores (Fig. 3).

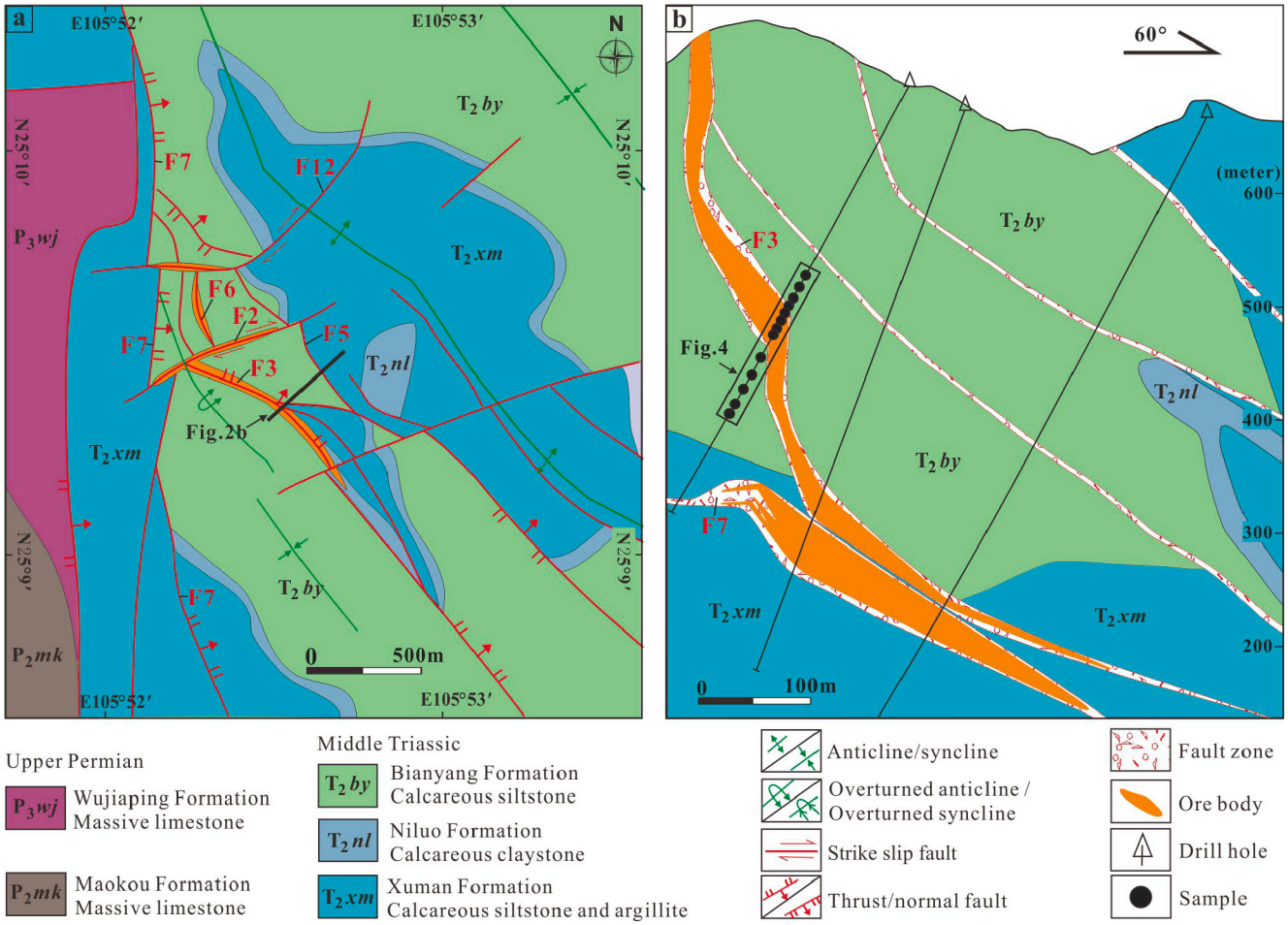

Fig. 2. (a) Geological map of the Lannigou Au deposit. (b) Geological cross-section of the Lannigou Au deposit showing the locations of the collected samples along a short transect.

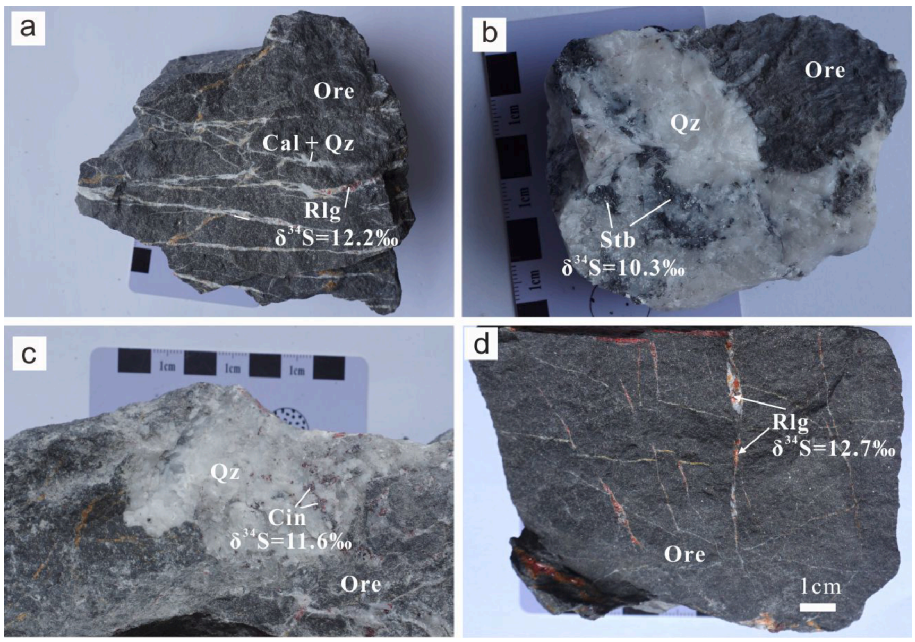

Fig. 3. Photographs of realgar, stibnite, and cinnabar coexisting with calcite and quartz veins in ore from the Lannigou Au deposit. The photographs show the bulk S isotope values of these sulfides. Abbreviations: Rlg = realgar; Stb = stibnite; Cin = cinnabar; Qz = quartz; and Cal = Calcite.

4. Material and methods

4.1. Material

A total of 13 whole-rock samples were collected from the drill core along a short transect (Fig. 2b). The drill log was examined to identify the sample transect across the high-Au-grade fault zone. The primary stratigraphic units and lithologies surrounding the ore-bearing fault zone were consistent, indicating that variations in the elements and minerals could be more confidently related to hydrothermal events. All samples were powdered under 200 mesh for major and trace element analyses. Additionally, the samples were polished into thin sections for subsequent petrographic observations and analyses.

4.2. Major and trace element analyses

The major and trace element compositions of the samples were analyzed at ALS Chemex (Guangzhou) Co. Ltd. The major elements were analyzed using a PANalytical Axios-advance X-ray fluorescence spectrometer (Axios PW4400). Loss on ignition (LOI) was calculated using 1 g of rock powder heated to 1,100 ℃ for 1 h. Trace elements were detected using an Agilent 7900 ICP-MS. Gold was first digested using the fire assay method and then analyzed using an Agilent 5110 inductively coupled plasma atomic emission spectrometer (with an Au content of 0.001–10 ppm). For high-grade samples (with an Au content of >10 ppm), the Au content was obtained using the gravimetric method. Mercury analysis was performed using an Agilent 7900 ICP-MS instrument. The analytical precision for all elements was >5%; Appendix A provides the detection limits.

4.3. Petrography observation

The polished thin sections were inspected using an optical petrographic Leica DM4P microscope equipped with an electric scanning platform at the Institute of Geochemistry, Chinese Academy of Sciences (IGCAS). The overall characteristics and textural relationships of the wall rock and ore were easily observable in the thin section scans. A thermal field-emission scanning electron microscope (FESEM, JEOL JSM-7800F) equipped with an energy dispersive spectrometer (EDS) at the IGCAS was used to observe mineral textures, identify minerals, and determine mineral paragenesis. Backscattered electron (BSE) images were captured to observe textures and provide precise locations for subsequent LA-ICP-MS and LA -MC-ICP-MS analyses.

4.4. Mineral phase mapping

Mineral mapping of the polished samples was obtained using the TIMA facilities at Guangzhou Tuoyan Analytical Technology Co., Ltd., comprising a MIRA3 SEM system with four EDS detectors. The analyses were conducted at a working voltage of 25 kV and a probe current of 10 nA. The working distance was set to 15 mm. The pixel spacing was set to 3 μm and the dot spacing was set to 9 μm. The current and BSE signal intensities were calibrated on a platinum Faraday cup using an automated procedure. The EDS performance was evaluated using a manganese standard. The samples were scanned using the TIMA liberation analysis module, which automatically calculated the volume ratios of all mineral phases.

4.5. Pyrite in situ trace element analysis

In situ LA-ICP-MS analyses of pyrite in the polished section were conducted at Nanjing FocuMS Technology Co., Ltd. A Teledyne Cetac Technologies Analyte Excite LA system was coupled to an Agilent Technologies 7700x quadrupole ICP-MS instrument. The 193 nm ArF excimer laser, homogenized by a set of beam delivery systems, was focused on the sulfide surface with a fluence of 3.5 J/cm^2. The ablated material was transported to the ICP-MS instrument by a He carrier gas. The United States Geological Survey (USGS) polymetallic sulfide pressed pellet, MASS-1, and synthetic basaltic glass, GSE-1G, were combined for external calibration. In this study, a single ablation was performed using a spot size of 20–40 μm at a repetition rate of 6 Hz for 30 s. Appendix provides the elemental detection limits.

4.6. Sulfur isotope analysis of sulfides

In situ sulfur isotope analyses of pyrite were conducted using LA-MC-ICP-MS at Nanjing FocuMS Technology Limited. A Teledyne Cetac Technologies Analyte Excite LA system and a Nu Instruments Nu Plasma

II MC-ICP-MS were combined for the experiments. The 193 nm ArF excimer laser, homogenized by a set of beam delivery systems, was focused on the surface with a fluence of 2.5 J/cm^2. Each acquisition incorporated a 30 s background (gas blank) collection, followed by a spot diameter of 33 μm at a 5 Hz repetition rate for 40 s. Natural pyrite Wenshan ($\delta^{34}S = +1.1‰$) was used as an external bracketing standard every fourth analysis. Pressed powder pellets of pyrite GBW07267 and chalcopyrite GBW07268 ($\delta^{34}S = +3.6$ and $-0.3‰$, respectively, from the National Research Center for Geoanalysis, China) and fine-grained sphalerite SRM 123 ($\delta^{34}S = +17.5‰$, from the National Institute of Standards and Technology, USA) were used for quality control. The long-term reproducibility of $\delta^{34}S$ was >0.6‰ (one standard deviation). The S isotope compositions of the separated sulfide minerals (stibnite, realgar, and cinnabar) were measured using the conventional combustion method. The analysis was conducted using a Thermo Fisher MAT-253 mass spectrometer at IGCAS. The analytical procedure was monitored by measuring the following reference materials: GBW04414, GBW04415, and IAEA-S3. Sulfur isotope data were reported with respect to the Vienna-Canyon Diablo Troilite (V-CDT).

5. Results

5.1. Major and trace elements

Appendix A provides the analyzed results for the major and trace element contents of the whole rock samples from the Lannigou deposit. Fig. 4 shows the elemental variations across the ore-bearing fault. The Carlin-suite elements (SO_3, Au, As, Sb, Hg, and Tl) and Ag displayed nearly consistent variations and significant enrichments in the orebody. Additionally, Mo, W, and SiO_2 contents increased while CaO, MgO, and Na_2O contents decreased with the increasing Au content. Contents of other elements (Co, Cu, Ni, Pb, Sn, Zn, Bi, TFe_2O_3, P_2O_5, K_2O, Al_2O_3, and TiO_2), marked in gray in Fig. 4, remained constant with variations in the Au content.

5.2. Mineral compositions

Table 1 and Fig. 5, respectively, present the mineral compositions and mappings of the polished wall rock and ore samples determined by TIMA. The exact positions of the TIMA analyses are marked on the hand specimen photographs (Fig. 5a, e) and reflected light scanning images of the thin sections (Fig. 5b, f). The reflected light photographs showed the differences in the pyrite content between the wall rock and ore. The mineral categories in the wall rock and ore were similar, but their contents differed significantly (Fig. 5c, d, g, h). The wall rock was mainly composed of quartz (59.153 vol%), illite (11.310 vol%), calcite (13.153 vol%), albite (9.458 vol%), Fe dolomite (4.275 vol%), and siderite (1.093 vol%). The ore was principally dominated by quartz (79.361 vol%), illite (15.117 vol%), Fe dolomite (2.596 vol%), and pyrite (1.275 vol%). Other minerals, including dolomite, kaolinite, rutile, apatite, schorl, chlorite, zircon, florencite, sphalerite, monazite, and arsenopyrite, were minor (<1 vol%) in the wall rock and ore.

The histogram of difference in terms of mineral contents in the wall rock and ore (Fig. 6) accurately displays the mineral variations related to the alterations and mineralization. The results showed that the amounts

Table 1
Statistical parameters of minerals in wall rock and ore from the Lannigou Au deposit.

Minerals	Wall rock (3–190)		Ore (3–226)	
	Vol.%	Grains No.	Vol.%	Grains No.
Quartz	59.153	33,510	79.361	17,833
Illite	11.310	126,200	15.117	140,623
Pyrite	0.021	350	1.275	29,044
Calcite	13.153	64,055	0.738	16,261
Albite	9.458	41,019	0.002	139
Fe dolomite	4.275	35,103	2.596	21,980
Siderite	1.093	18,418	0.003	62
Dolomite	0.321	1628	0.429	2446
Kaolinite	0.697	14,196	0.039	2612
Rutile	0.141	3887	0.173	4698
Apatite	0.127	1569	0.163	1682
Schorl	0.148	2481	0.063	355
Chlorite	0.078	4573	0.000	27
Zircon	0.013	141	0.025	199
Florencite	0.003	69	0.005	4573
Sphalerite	0.002	38	0.003	73
Monazite	0.001	10	0.001	15
Arsenopyrite	0.000	0	0.002	140
Unclassified	0.003	737	0.003	767

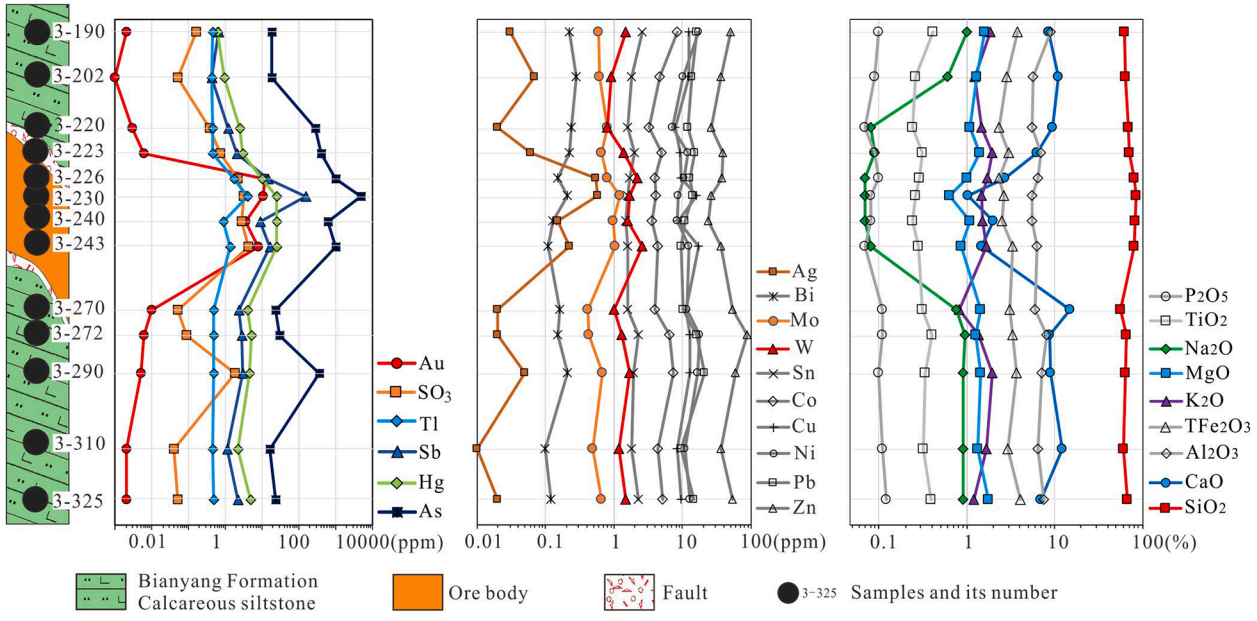

Fig. 4. Variations in the major and trace elemental compositions along a short transect at the Lannigou Au deposit. Fig. 2b shows the location of the transect. Arsenic, Sb, Hg, Tl, Ag, SO_3, and SiO_2 contents notably increase; the Mo and W contents increase insignificantly; and the CaO, MgO, and Na_2O contents decrease with an increasing Au grade.

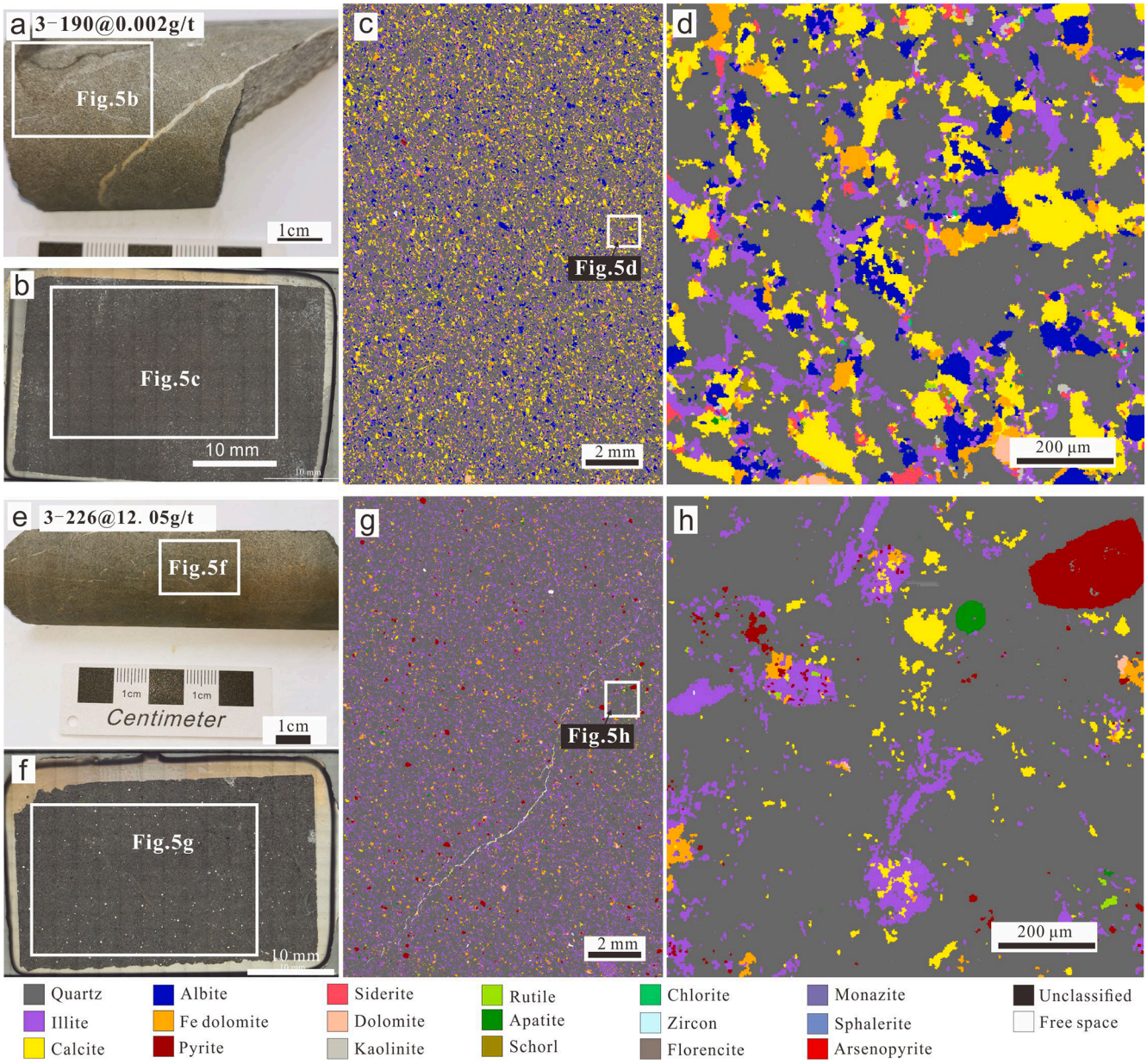

Fig. 5. Hand specimen photographs, reflected light scanning images, and mineral maps of the wall rock (a–d) and ore (e–h) samples. The wall rocks primarily consist of quartz (gray), calcite (yellow), illite (purple), albite (blue), Fe dolomite (Au yellow), and siderite (pink). The ore mainly consists of quartz, illite, Fe dolomite, and pyrite (dark red).

of quartz, illite, and pyrite significantly increased while that of calcite, albite, Fe dolomite, and siderite were depleted in the ore. We note that 140 grains of arsenopyrite were discovered in the ore but were scarce in the wall rock.

5.3. Pyrite types and morphologies

Pyrite is the primary pre-ore sulfide and ore-stage Au-carrying mineral in the Lannigou deposit. Based on the morphology, texture, and geochemistry of pyrite, five distinct pyrite types were observed: pyrite 1 (Py1), 2 (Py2), 3 (Py3), 4 (Py4), and ore pyrite (OPy). Py1 (Fig. 7a, b), Py2 (Fig. 7c, d), and Py3 (Fig. 7e, f) were mainly observed in the wall rock, whereas Py4 and OPy were only discovered in the ore (Fig. 7g–l).

Py1 was framboidal, consisting of spherical or euhedral pyrite crystallites (~0.5–1 μm in diameter) separated by pore space. The diameter of a single framboidal pyrite sample was approximately 5–30 μm. This pyrite was yellowish-white, poorly polished, and usually occurred as an aggregation of framboidal pyrite. Some of the Py1 grains were cemented by later generations of pyrite that formed during the diagenetic stage. Py2 was mainly subhedral or euhedral and was approximately 30–50 μm in diameter. It was easily identifiable under an optical microscope, as it was yellowish-white and well-polished, with a bright reflectivity and high relief. Py3 was commonly nodular or bioclastically aggregated, with a diameter of ~30–80 μm, and composed of fined-grain spherical or euhedral pyrite crystals (~5 μm in diameter). Some fine-grained crystals were chemically distinct, showing grayish-white spots in BSE images.

Pyrite in the ore was mostly coarse-grained and displayed a distinct zoned texture, with Py4 in the core and OPy in the rim. Py4 and OPy were easily discriminated under an optical microscope and in BSE imaging when adjusted for low brightness and high contrast. Py4 was yellowish-white and poorly polished under an optical microscope and dark gray in BSE images, whereas OPy was light golden-yellow and well-polished under an optical microscope and bright gray in BSE images. Py4 was commonly 40–100 μm in diameter and usually contained many

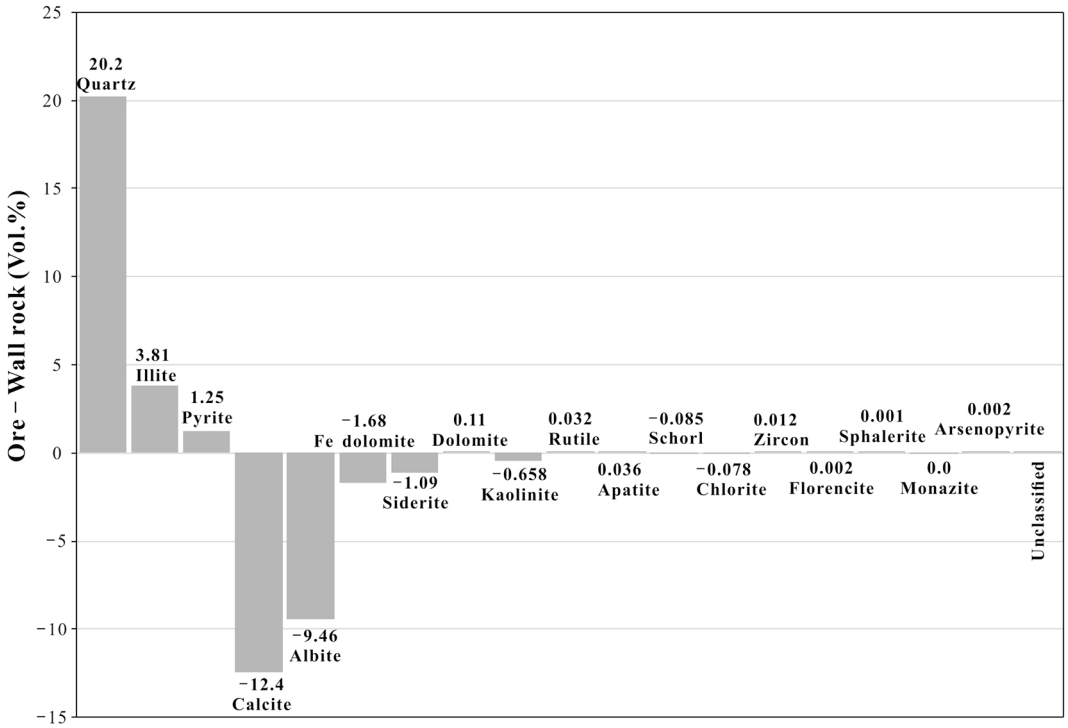

Fig. 6. The histogram of difference values of mineral contents in the wall rock and ore from the Lannigou deposit. Compared with the wall rock, quartz, illite, and pyrite significantly increase, whereas calcite, albite, Fe dolomite, and siderite decrease in the ore.

illite or quartz inclusions and fractures, which were scarce in OPy.

OPy was the dominant Au-bearing mineral in the ore and represented ore stage pyrite. OPy was usually 10–60 μm thick and contained multiple As-rich sub-bands, which were too narrow for analysis via LA-ICP-MS and LA-MC-ICP-MS. Additionally, OPy also formed individual subhedral to euhedral fine-grained pyrite, with a diameter of ~5–20 μm. The fine-grained OPy was usually a pyritohedron and contained multiple As-rich sub-bands in BSE imaging (Fig. 7i), which was easily distinguished from subhedral or euhedral Py2 (Fig. 7c, d).

5.4. Trace element compositions of pyrite

A total of 12 trace elements in pyrite were obtained using LA-ICP-MS, including Au, As, Sb, Tl, Ag, Cu, Pb, Co, Ni, Mn, Zn, and Mo. The obtained values were mainly higher than 3-fold the detection limit. Appendix B provides the LA-ICP-MS data for pyrite, which are shown in Fig. 8. Table 2 lists the statistical medians and averages of the trace elements in the pyrite.

Py1, Py2, and Py3 were characterized by relatively high Co, Ni, Mn, Zn, and Mo contents (Fig. 8; median values ranging from 10 to 1,000 ppm). However, they showed minor differences. Py1 had elevated concentrations of Au (0.384 ppm), Tl (6.13 ppm), Ag (17.3 ppm), and Pb (689 ppm) compared with that of Py2 and Py3, which contained 0.070 and 0.073 ppm of Au, 0.789 and 0.741 ppm of Tl, 3.53 and 3.32 ppm of Ag, and 89.2 and 132 ppm of Pb, respectively. In contrast, the Zn contents were low in Py1 (21.1 ppm), whereas they were high in Py2 (111 ppm) and Py3 (75.3 ppm).

The trace element contents in Py4 and OPy showed apparent differences and similarities (Fig. 8). Higher ore-related element contents in OPy (Au of 58.6 ppm, As of 51 863 ppm, Sb of 366 ppm, Tl of 12.4 ppm, and Cu of 1038 ppm) reflected these differences as compared to those in Py4 (Au of 0.122 ppm, As of 831 ppm, Sb of 60.2 ppm, Tl of 0.446 ppm, and Cu of 29.1 ppm). The contents of Pb (359 ppm), Co (27.2 ppm), Ni (131 ppm), Mn (2.11 ppm), Zn (0.710 ppm), and Mo (0.010 ppm) in Py4 were similar to those in OPy (Pb of 356 ppm, Co of 6.69 ppm, Ni of 46.2 ppm, Mn of 0.262 ppm, Zn of 1.51 ppm, and Mo of 0.010 ppm), but differed from those in Py1, Py2, and Py3. Additionally, the Sb content in Py4 (60.2 ppm) was lower than that in OPy (366 ppm), but higher than that in Py1 (27.4 ppm), Py2 (18.2 ppm), and Py3 (11.9 ppm). Collectively, the trace element compositions of Py4 resembled those of OPy, except for ore-related elements (Au, As, Sb, Tl, and Cu).

5.5. S isotope compositions of sulfides

Appendix C provides the *in situ* S isotope compositions of pyrite and the bulk S isotope values of stibnite, realgar, and cinnabar, which are shown in Fig. 9. The $\delta^{34}S$ values of Py1, Py2, and Py3 showed significant variations, ranging from −5.1 to 35.4‰, with an average of 15.4‰. Specifically, the obtained $\delta^{34}S$ values for Py1 were 8.6 and 9.2‰, 32.5 and 35.4‰ for Py2, and 11.8 and −5.1‰ for Py3. The S isotope results for Py4 and OPy all displayed narrow ranges. Py4 yielded $\delta^{34}S$ values varying from 7.6 to 13.3‰ with an average of 9.1‰, while OPy yielded $\delta^{34}S$ values from 9.4 to 14.1‰, with an average of 12.4‰. Additionally, the bulk S isotope values of realgar, stibnite, and cinnabar, which are the dominant late ore-stage sulfides coexisting with calcite and quartz veins in the orebodies (Fig. 3), ranged from 10.0 to 12.7‰, with an average of 11.6‰, similar to the S isotope range of OPy.

6. Discussion

6.1. Pyrite formation

Py1, Py2, and Py3 were mainly observed in the wall rock; however, the wall rock samples lacked Au (0.002 ppm) and showed no hydrothermal alteration or mineralization, indicating that Py1, Py2, and Py3 formed before Au mineralization. Typical global sedimentary (diagenetic or syngenetic) pyrite, as determined by Large et al. (2014) and Gregory et al. (2015), has framboidal, nodular, and fine euhedral microcrystal textures, containing abundant As, Ni, Pb, Cu, and Co contents (medians ranging from 100 to 1,000 ppm) and high Mo, Sb, Zn, and Se contents (medians ranging from 10 to 100 ppm). Py1, Py2, and Py3 exhibited textural and chemical similarities (Fig. 7a–f and Fig. 8;

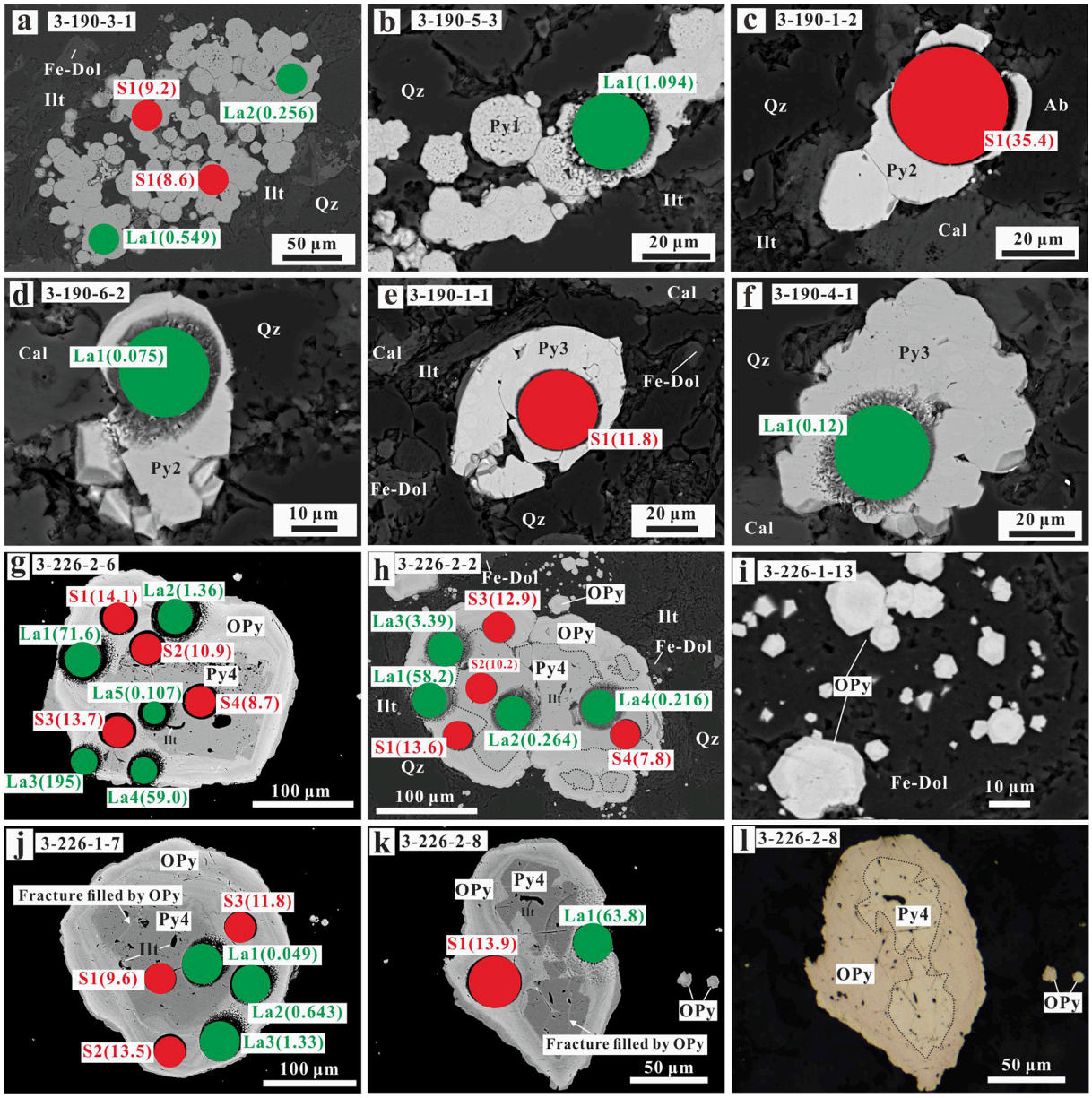

Fig. 7. BSE (a–k) and reflected light (l) images of pyrite in the wall rock and ore from the Lannigou Au deposit. Pyrite in the wall rock (a–f) shows framboidal, nodular, and fine euhedral microcrystal textures while pyrite in the ore (g–k) have zoned textures showing a core that is darker than the rim. Pyrite cores intersected by bright pyrite contain large amounts of illite or quartz inclusions,. Green and red dots in the images indicate the locations of the LA-ICP-MS and LA-MC-ICP-MS analyses, respectively. Analytical results for Au concentration (ppm) and $\delta^{34}S$ isotope values (‰) are denoted with the analysis number. Appendices B and C list all of the LA-ICP-MS and LA-MC-ICP-MS data, respectively. Abbreviations: Fe-Dol = Fe dolomite; Ilt = illite; Qz = quartz; Cal = Calcite; Ab = Albite; Py1 = pre-ore pyrite 1; Py2 = pre-ore pyrite 2; Py3 = pre-ore pyrite 3; Py4 = pre-ore pyrite 4; OPy = ore pyrite.

Table 2) to typical sedimentary pyrite, consistent with their sedimentary origin. Additionally, Py1, Py2, and Py3 displayed a wide range of $\delta^{34}S$ values from −5.1 to 35.4‰, implying that these pyrites likely formed via bacterial sulfate reduction during sedimentation and diagenesis in (semi-) open and sulfate-limited systems (Aharon and Fu, 2000; Shen et al., 2001). The non-presence of Py1, Py2, and Py3 in the ore could be attributed to corrosion or dissolution during hydrothermal activities after the syngenetic and diagenetic stages.

Py4 and OPy were the primary pyrite in the ore. Pyrite in the wall rocks was rare (0.021 vol%, Table 1) while pyrite significantly increased in the ore (1.275 vol%, Table 1), indicating that Py4 and OPy formed via hydrothermal processes after the syngenetic and diagenetic stages, although minor sedimentary pyrite may have been retained in the ore. The chemistry of Py4 was similar to that of OPy in terms of their low Co, Ni, Mn, Zn, and Mo contents, but differed from that of typical sedimentary pyrite (Fig. 8; Large et al., 2014; Gregory et al., 2015), indicating that Py4 and OPy all had hydrothermal origins. The S isotope composition of Py4 displayed a narrow range (from 7.6 to 13.3‰), suggesting that S in Py4 was sourced from a hydrothermal fluid with a uniform S isotopic composition in contrast to sedimentary pyrite, which commonly shows a broad range of S isotope values (Hou et al., 2016; Jin, 2017; Li et al., 2019; 2020; Liang et al., 2020). Additionally, Py4 was commonly coarse-grained euhedral with flat edges (Fig. 7g–l), which is significantly different from typical sedimentary pyrite exhibiting framboidal, nodular, and fine euhedral microcrystal textures (Fig. 7a–f; Large et al., 2014; Gregory et al., 2015). In other words, Py4 had textural and chemical affinities to typical hydrothermal pyrite, implying a hydrothermal origin.

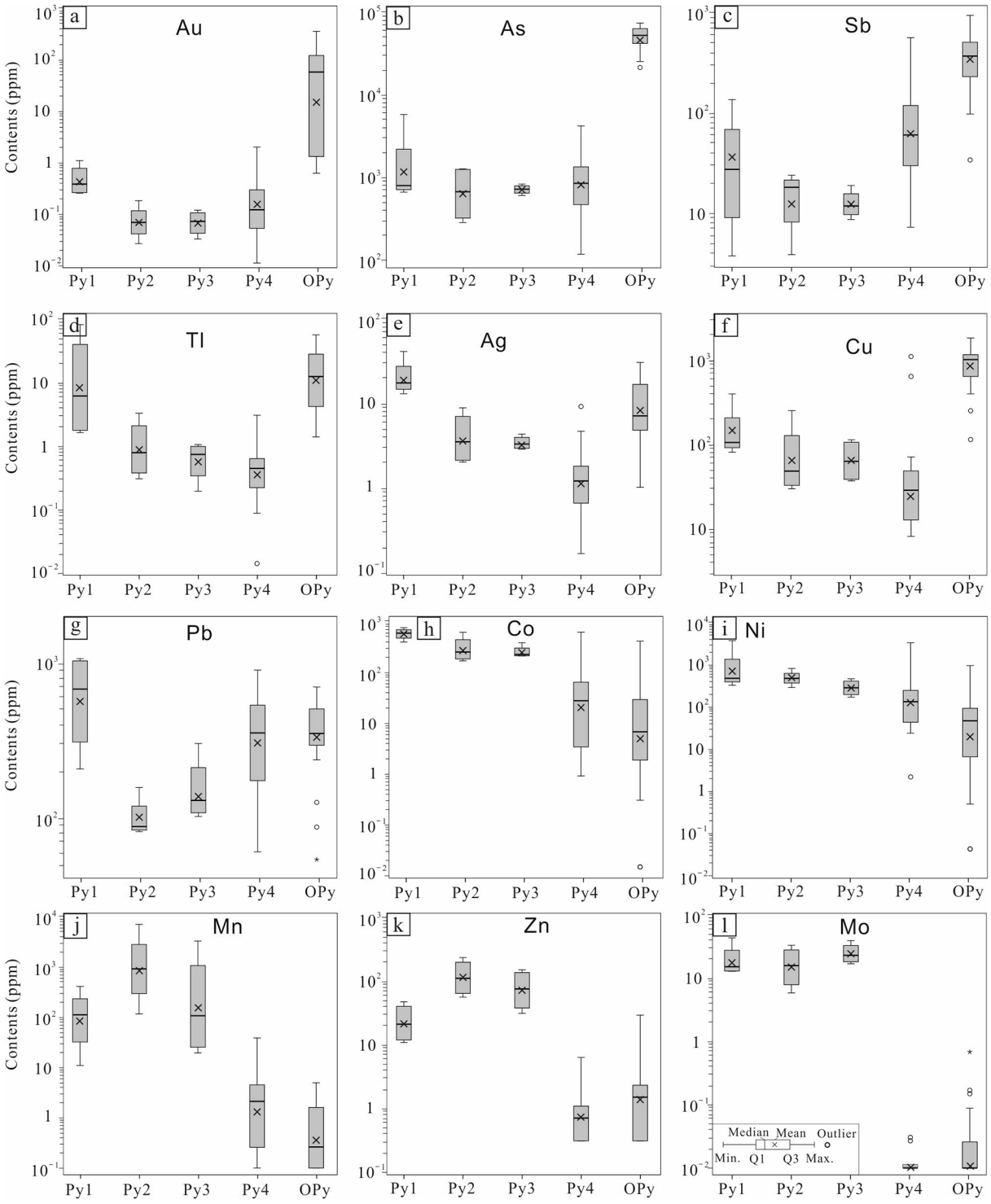

Fig. 8. Box-plots showing the LA-ICP-MS data (Appendix B) for pyrite for Au (a), As (b), Sb (c), Tl (d), Ag (e), Cu (f), Pb (g), Co (h), Ni (i), Mn (j), Zn (k), and Mo (l) from the Lannigou Au deposit. The data were logarithmically transformed prior to plotting. Abbreviations: Py1 = pre-ore pyrite 1; Py2 = pre-ore pyrite 2; Py3 = pre-ore pyrite 3; Py4 = pre-ore pyrite 4; OPy = ore pyrite.

The elevated concentrations of Au, As, Sb, and Tl in OPy (Fig. 8) accounted for the addition of these elements into the mineralized rock (Fig. 4). While the Fe content was constant, a significant amount of S was introduced into the ore (Fig. 4), demonstrating that sulfidation, rather than pyritization, accounted for the formation of hydrothermal pyrite in the ore, similar to other Carlin-type Au deposits in southwestern China and Nevada, USA (Hofstra and Cline, 2000; Cail and Cline, 2001; Tan et al., 2015; Su et al., 2018). Mineral variations related to alteration and mineralization showed an observable depletion of Fe dolomite and siderite in the ore (Figs. 5 and 6), suggesting that their dissolution provided Fe to form hydrothermal pyrite in the ore.

6.2. *Two episodes of hydrothermal pyrite*

The above mineralogical and geochemical characteristics show that Py4 had a hydrothermal origin. However, whether Py4 formed from a

Table 2
Median and average of trace elements in pyrite from the Lannigou deposit determined using LA-ICP-MS (ppm).

Type	Au	As	Sb	Tl	Ag	Cu	Pb	Co	Ni	Mn	Zn	Mo
	Median											
Py1	0.384	779	27.4	6.13	17.3	107	689	598	469	110	21.1	14.9
Py2	0.070	657	18.2	0.789	3.53	48.9	89.2	245	467	901	111	15.6
Py3	0.073	706	11.9	0.741	3.32	64.1	132	220	280	108	75.3	22.6
Py4	0.122	831	60.2	0.446	1.22	29.1	359	27.2	131	2.11	0.710	0.010
OPy	58.6	51,863	366	12.4	7.11	1038	356	6.69	46.2	0.262	1.51	0.010
	Average											
Py1	0.450	1224	24.9	8.39	19.9	140	574	576	714	86	21.9	18.6
Py2	0.070	621	13.3	0.890	3.87	65.6	101	277	472	895	113	14.6
Py3	0.068	700	12.4	0.581	3.42	65.0	153	247	278	166	71.8	24.0
Py4	0.144	809	64.0	0.358	1.10	35.0	307	20.3	124	1.25	0.765	0.011
OPy	18.9	47,857	321	10.2	8.25	808	330	4.70	19.8	0.394	1.24	0.019

Notes: Data used to calculate the median and average are listed in Appendix B. Half of the detection limit was used if the result was below the detection limit during the calculation.
Abbreviations Py1 = pre-ore pyrite 1, Py2 = pre-ore pyrite 2, Py3 = pre-ore pyrite 3, Py4 = pre-ore pyrite 4, OPy = ore pyrite.

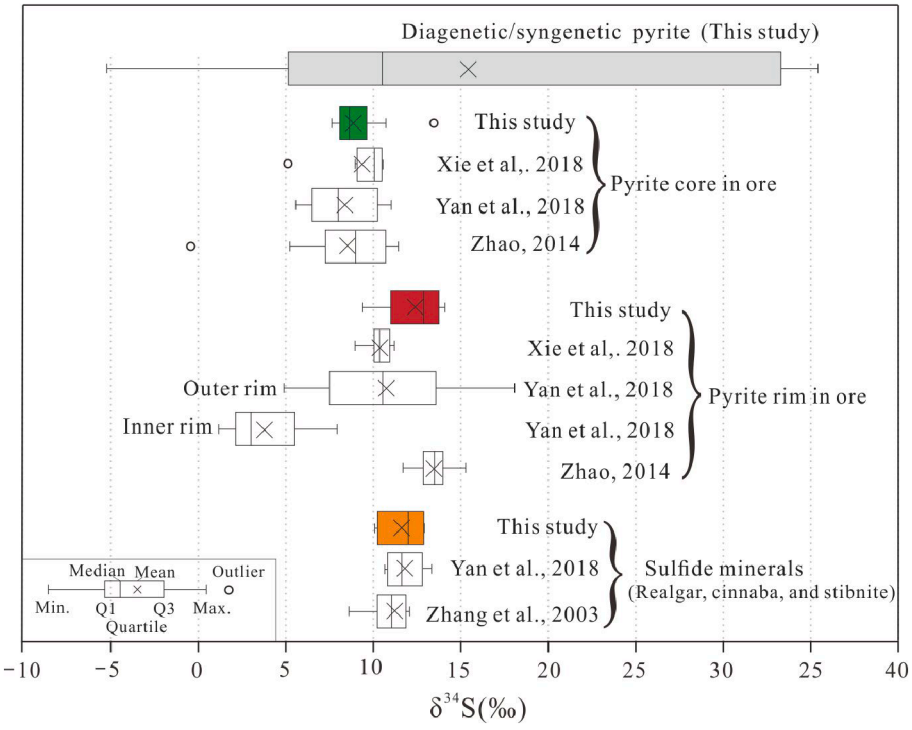

Fig. 9. Box-plots of the available $\delta^{34}S$ isotope data for the Lannigou Au deposit. Pyrite was analyzed using *in situ* techniques, including SHRIMP, LA-MC-ICP-MS, and NanoSIMS. Late ore-stage sulfide minerals were analyzed using bulk techniques.

pre-ore hydrothermal fluid or during the early stage of the ore-forming fluid remains unclear. Here, we propose a hypothesis where Py4 sedimented from a pre-ore hydrothermal event. The major evidence supporting this hypothesis is as follows.

6.2.1. Mineralogical features

The texture characteristics of Py4 and OPy were significantly different in the Lannigou deposit (Fig. 7g–l). Numerous Py4 grains were fractured and filled by OPy, whereas fractures were lacking in OPy. The fractures in Py4 implied an episode of tectonic stress after Py4 sedimentation before ore-stage hydrothermal activity. Additionally, Py4 commonly contained a significant number of illite or quartz inclusions, which were scarce in OPy. Pre-ore Py4 may have been corroded and altered by later ore fluids leaving abundant pores filled by ore-stage gangue minerals. Lastly, Py4 was homogeneous, but OPy contained multiple As-rich sub-bands. The sub-bands likely resulted from the episodic incursion of Au- and As-rich fluids into the hydrothermal system (Barker et al., 2009); however, such fluid pulses were absent in the Py4 hydrothermal system. OPy also formed individual subhedral to euhedral fine-grained pyrite (Fig. 7i), which only contained multiple As-rich sub-bands, but no barren pyrite cores. These mineralogical features indicate that Py4 likely sedimented from a pre-ore hydrothermal fluid, but not at the early stage of ore-forming fluids.

Zoned pyrite like that in the Lannigou deposit are also universal in other Carlin-type Au deposits in the Youjiang Basin (Fig. 10; Jin, 2017; Hu et al., 2018; Li, 2019; Li et al., 2019; 2020; Zhao et al., 2019; He et al., 2021; Lin et al., 2021; Song et al., 2022; under review). Similarities include homogeneous and fractured pyrite cores containing abundant illite or quartz inclusions and rhythmic pyrite rims containing multiple Au-rich sub-bands. The pyrite rims from most of the Au deposits can be roughly divided into As-rich inner rims (bright gray in BSE image) and relatively As-low outer rims (gray in BSE image), indicating

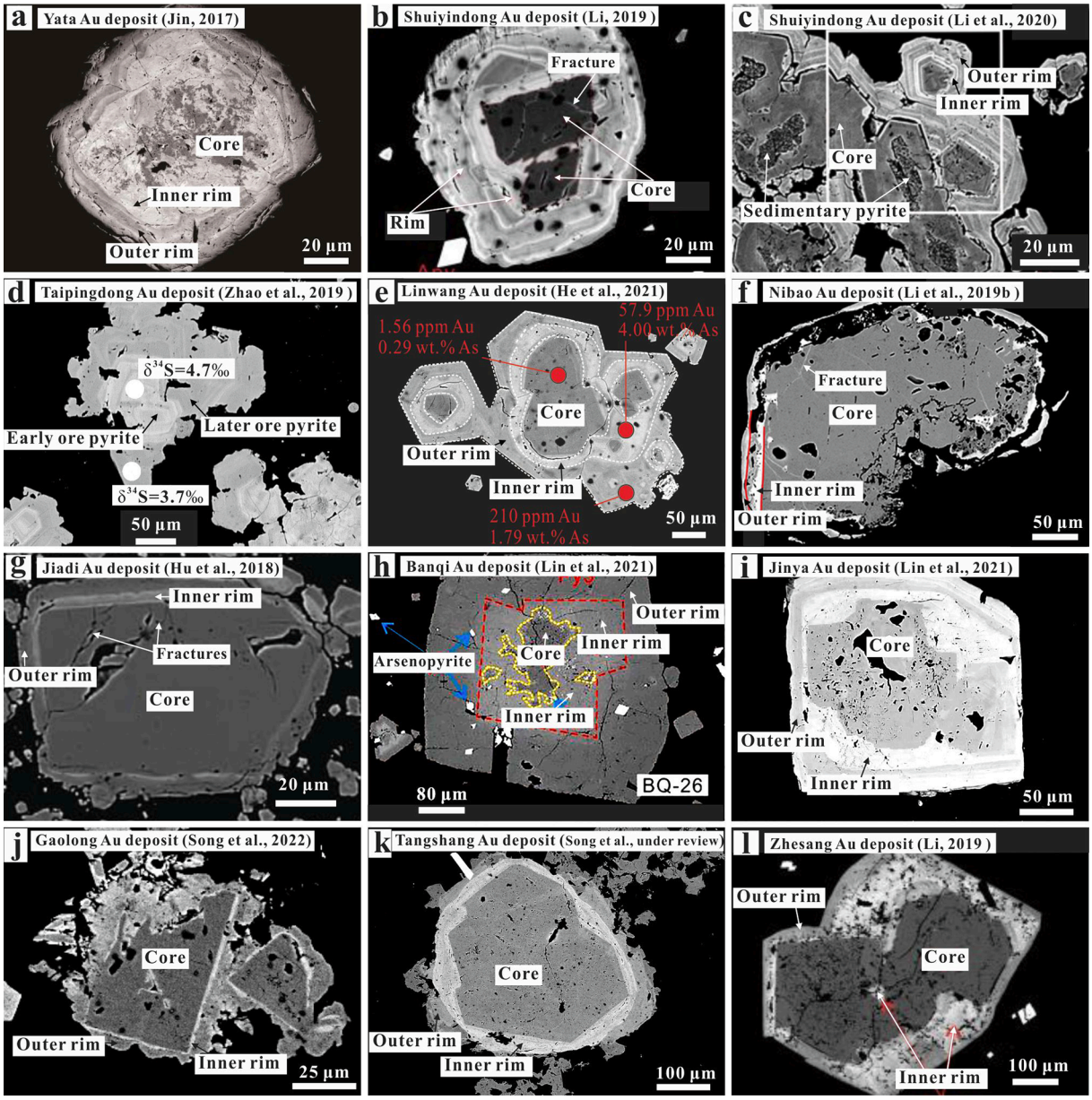

Fig. 10. BSE images of pyrite in the ore from other Carlin-type Au deposits in the Youjiang Basin.

that the ore-forming fluids for these deposits may have experienced similar evolution processes. Additionally, single euhedral coarse-grained ore pyrite with a diameter of > 100 μm (Fig. 10d) was also observed in the Taipingdong Au deposit (Zhao et al., 2019). The single ore pyrite, containing multiple sub-bands, showed early As-rich and later relatively As deficient ore pyrite, corresponding to the bright gray inner rims and gray outer rims of the zoned pyrite, respectively. Ore pyrite likely not only grew around pre-ore coarse-grained pyrite, but was also sedimented based on the ore-stage pyrite nuclei. Collectively, pre-ore hydrothermal pyrite is ubiquitous in the Carlin-type Au deposits in the Youjiang Basin, implying large-scale pre-ore hydrothermal activity in the basin.

6.2.2. *Chemical differences*

Although the Co, Ni, Mn, Zn, and Mo contents in Py4 and OPy were similar in the Lannigou deposit, the contents of the Carlin-suit elements (Au, As, Sb, Tl, and Cu) in Py4 were significantly below those in OPy (Fig. 8). The $\delta^{34}S$ values of Py4 displayed a narrow range from 7.6 to 13.3‰, implying a hydrothermal origin (Fig. 9), however, the average $\delta^{34}S$ value of Py4 (9.1‰) was lower than that of OPy (12.4%). Zhao (2014), Xie et al. (2018b), and Yan et al. (2018) also reported similar S isotopic differences in the pyrite cores and rims in the Lannigou deposit (Fig. 9). NanoSIMS analyses by Yan et al. (2018) especially provided broad $\delta^{34}S$ values (1.1–18.1‰) for pyrite rims and a relatively narrow range of $\delta^{34}S$ values (6–12‰) for pyrite cores. This phenomenon is consistent with the texture characteristics where Py4 is commonly homogeneous and OPy generally contains multiple As-rich sub-bands.

Pyrite cores and rims from other Au deposits in the Youjiang Basin also exhibit notable chemical differences (Zhao, 2014; Hou et al., 2016; Jin, 2017; Hu et al., 2018; Xie et al., 2018b; Yan et al., 2018; Li et al., 2019; 2020; Liang et al., 2020; Wei et al., 2020; Zhao et al., 2020; He et al., 2021; Lin et al., 2021; Song et al., 2022; under review). Published *in situ* trace element contents (represented by Au and Co) and S isotope data on pyrite from other Au deposits in the Youjiang Basin were compiled and plotted in Figs. 11 and 12, respectively. For the three layers of zonal pyrite in the Shuiyindong deposits (Fig. 10c; Li et al., 2020), the inner cores were classified as sedimentary pyrite, whereas the middle part was interpreted as a pyrite core identified in this study. The

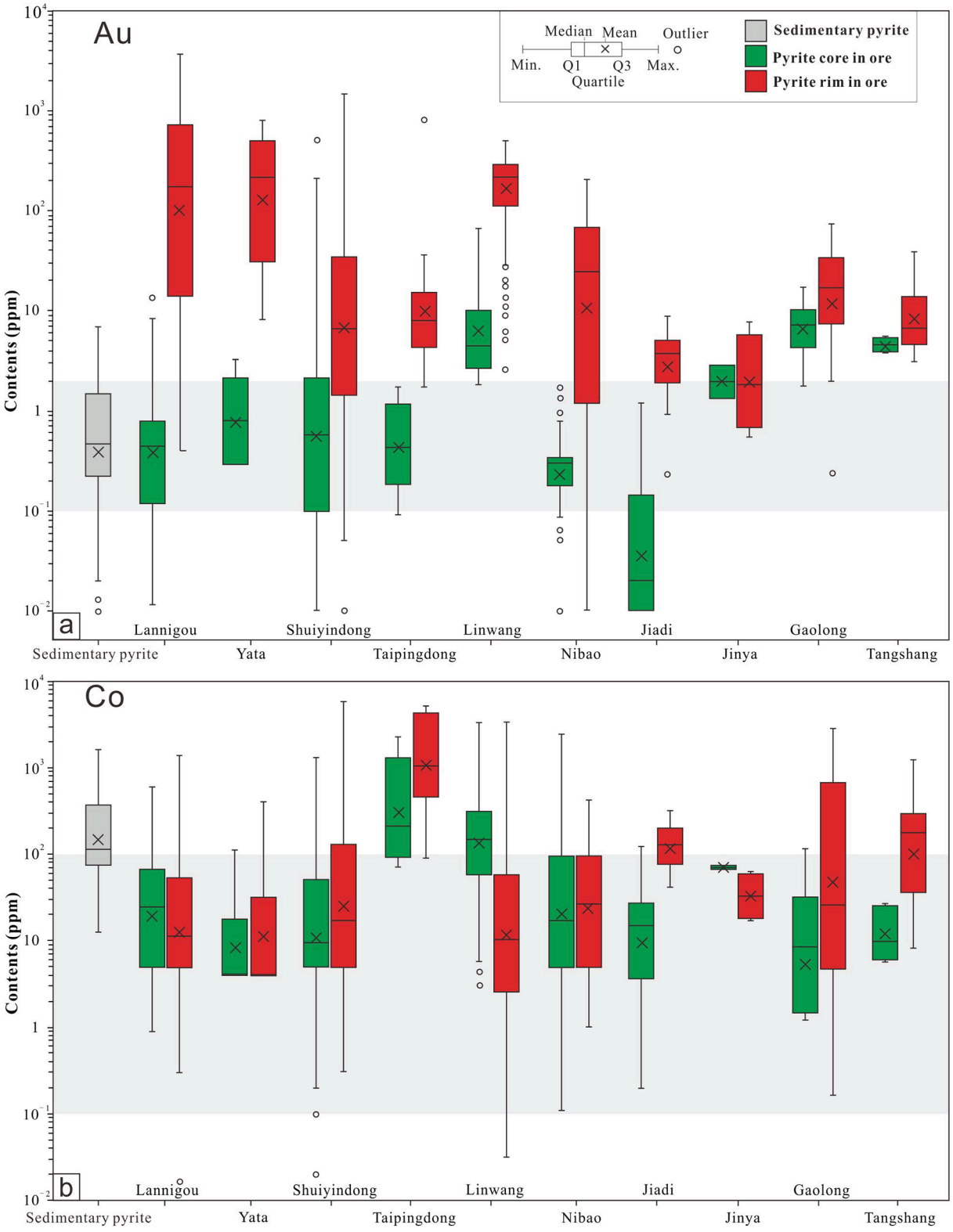

Fig. 11. Box plots of the Au (a) and Co (b) contents in zoned pyrite from the Carlin-type Au deposits in the Youjiang Basin. The gray box is sedimentary pyrite while the green and red boxes are pyrite cores and rims, respectively. Data compiled from Zhao (2014), Hou et al. (2016), Jin (2017), Hu et al. (2018), Xie et al. (2018b), Li et al. (2019; 2020), Wei et al. (2020), He et al. (2021), Lin et al. (2021), Song et al. (2022; Under Review), and this study. The data were logarithmically transformed prior to plotting.

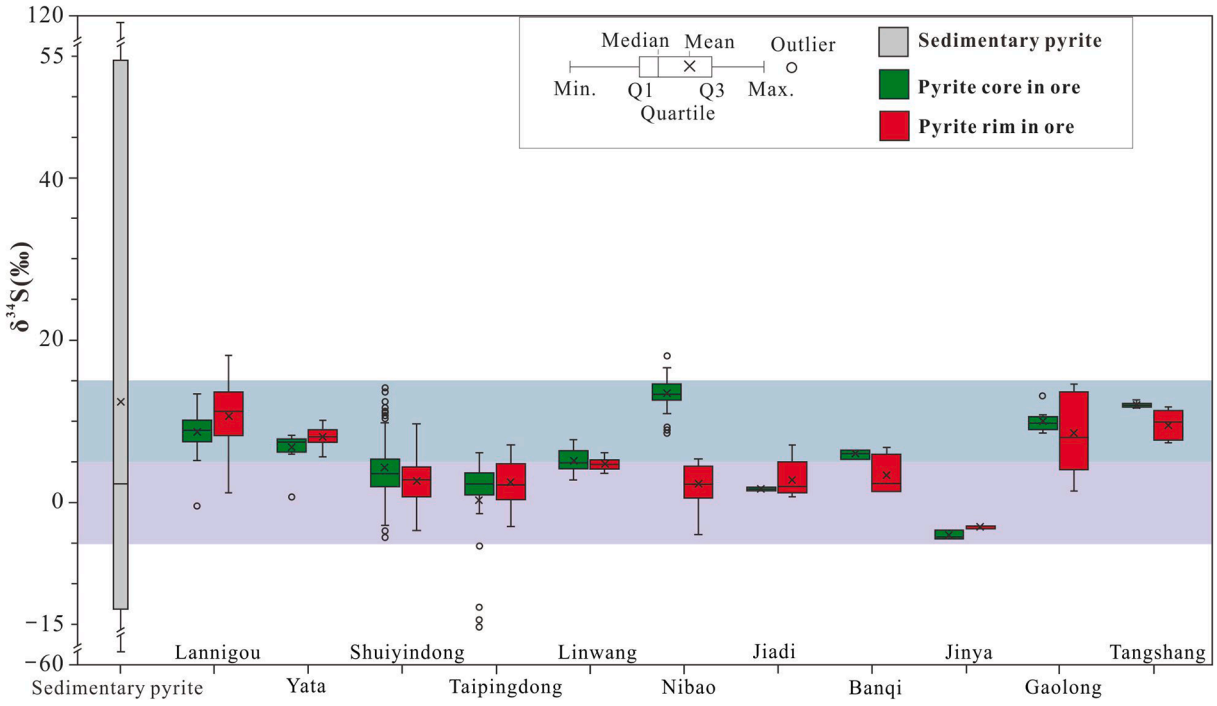

Fig. 12. Box plots of the $\delta^{34}S$ isotope values of zoned pyrite from Carlin-type Au deposits in the Youjiang Basin. The gray box is sedimentary pyrite while the green and red boxes represent pyrite cores and rims in ore, respectively. Data are from *in situ* techniques including SHRIMP, LA-MC-ICP-MS, and nanoSIMS only. Data compiled from Zhao (2014), Hou et al. (2016), Jin (2017), Hu et al. (2018), Xie et al. (2018b), Yan et al. (2018), Li et al. (2019; 2020), Liang et al. (2020), Wei et al. (2020), Zhao et al. (2020), He et al. (2021), Lin et al. (2021), Song et al. (2022; Under Review), and this study.

Au contents of the pyrite cores were significantly lower than that in the pyrite rims from most Au deposits in the Youjiang Basin (Fig. 11a). The Co contents in the pyrite cores and rims were roughly consistent in the Lannigou, Yata, Shuiyindong, and Nibao Au deposits, but were significantly different in the Taipingdong, Linwang, Jiadi, Gaolong, and Tangshang Au deposits (Fig. 11b). The high Co contents in the pyrite cores or Au-rich pyrite rims from the Taipingdong, Linwang, Jiadi, Gaolong, and Tangshang Au deposits may derive from water-rock reactions with local basic rocks (e.g., Emeishan basalt, tuff, and diabase). Additionally, the $\delta^{34}S$ values of the pyrite cores and rims from most of the Au deposits exhibited significant differences (Fig. 12). The average $\delta^{34}S$ values of the pyrite cores were higher or lower than that of the pyrite rims. The pyrite rims usually showed a wide range of $\delta^{34}S$ values, whereas the pyrite cores commonly had a relatively narrow range of $\delta^{34}S$ values for most Au deposits in the Youjiang Basin.

Collectively, the notable chemical differences in the pyrite cores and rims from the Lannigou and other Au deposits in the Youjiang Basin likely imply the possibility that zoned pyrite sedimented during two hydrothermal system episodes. Although ore-forming fluid pulses can also result in elemental and isotopic fluctuations in different stages of ore pyrite, the substantial mineralogical differences between the pyrite cores and rims exclude the possibility that the pyrite cores precipitated during the early stage of the ore-forming fluid.

6.2.3. *Two geochronological clusters*

The most reliable methods for restricting regional tectonic and related mineralization events are based on cross-cutting relationships. The youngest stratum that hosts Au orebodies in the Youjiang Basin is the Middle Triassic (approximately 247 Ma), corresponding to the maximum age limit for Au mineralization (Su et al., 2018). Additionally, the orebodies in the Liaotun Au deposit, Guangxi Autonomous Region, were cut by unaltered quartz porphyry dikes. A $^{40}Ar/^{39}Ar$ plateau age of 95.5 ± 0.7 Ma was confirmed for muscovite phenocrysts from the dike, which was interpreted as the minimum age limit for Au mineralization (Chen et al., 2014).

In the past two decades, abundant reliable geochronology data (247–95.5 Ma) on hydrothermal minerals coeval with Au mineralization have been obtained for the Carlin-type Au deposits in the Youjiang Basin (Liu et al., 2006; Chen et al., 2007; 2009; 2015; 2019; Su et al., 2009b; Pi et al., 2016; 2017; Dong, 2017; Hu et al., 2017; Jin, 2017; Gao, 2018; Tan et al., 2019; Zheng et al., 2019; Gao et al., 2021; Ge et al., 2021; Jin et al., 2021; Wang et al., 2021). These ages were compiled (see Appendix D), as plotted in Fig. 13. Two groups of ages can be observed in Fig. 13: approximately 130–150 and 200–230 Ma, implying two episodes of low-temperature metallogenesis (Hu et al., 2017).

Su et al. (2018) suggested that Au deposits in the northern Youjiang Basin (e.g., Shuiyindong and Nibao) formed via an Early Cretaceous hydrothermal event (130–150 Ma) while Au deposits in the southern

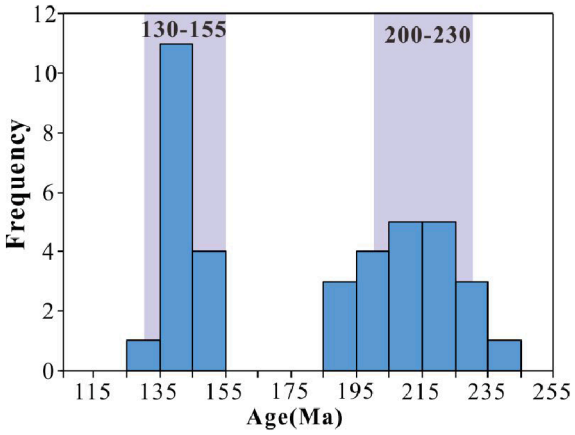

Fig. 13. Histogram of reliable ages from Carlin-type Au deposits in the Youjiang Basin (Liu et al., 2006; Chen et al., 2007; 2009; 2015; 2019; Su et al., 2009b; Pi et al., 2016; 2017; Dong, 2017; Hu et al., 2017; Jin, 2017; Gao, 2018; Tan et al., 2019; Zheng et al., 2019; Gao et al., 2021; Ge et al., 2021; Jin et al., 2021; Wang et al., 2021).

part of the basin (e.g., Zhesang and Anna) sedimented during a Late Triassic hydrothermal event (200–230 Ma). However, new ages on hydrothermal minerals from several Au deposits in the Youjiang Basin have revealed that the Late Triassic and Early Cretaceous hydrothermal events occurred across the basin. In the northern part of the basin, Huang et al. (2019) applied zircon and apatite fission-track and zircon (U–Th)/He methods to several Au deposits in the northern Youjiang Basin (Shuiyindong, Taipingdong, Yata, and Getang). From 247 to 95.5 Ma, they obtained two groups of thermochronological ages, i.e., 192–216 and 132–160 Ma, which record two episodes of geological thermal events (Huang et al., 2019). Additionally, three types of calcite have been observed in the Shuiyindong deposit based on cross-cutting relationships, cathodoluminescence colors, and chemical features. Furthermore, *in situ* U–Pb dating yielded calcite ages of 204.3–202.6, 191.9, and 139.3–137.1 Ma (Jin et al., 2021). In the southern part of the basin, hydrothermal sericite and rutile grains associated with Au-bearing sulfides in the Zhesang Au deposit yielded a $^{40}Ar/^{39}Ar$ age of 215.3 ± 1.9 Ma (Pi et al., 2016) and a U–Pb age of 213.6 ± 5.4 Ma, respectively (Pi et al., 2017). Hydrothermal rutile and monazite coeval with Au mineralization in the Badu Au deposit yielded a U–Pb age of 141.7 ± 5.8 Ma and a Th–Pb age of 143.5 ± 1.4 Ma, respectively (Gao et al., 2021).

Collectively, Carlin-type Au deposits in the Youjiang Basin likely experienced two episodes of hydrothermal events associated with the Late Triassic Indochina orogeny and Early Cretaceous Yanshanian orogeny. These two hydrothermal events may have contributed to the formation of zoned pyrite in the Carlin-type Au deposits in the Youjiang Basin. Although there is a lack of precise ages on Au-bearing minerals, the cross-cutting relationships between the pyrite cores and Au-rich rims constrain their age to the Early Cretaceous, which was likely the primary Au mineralization period in the Youjiang Basin.

6.3. Origins of hydrothermal fluids

The S isotope fractionation between pyrite and hydrothermal fluids is <2‰ (Ohmoto, 1972) under the fluid conditions in the Carlin-type Au deposits in the Youjiang Basin (low temperature: 190 to 300 °C; low fO_2; acidic to neutral H_2S-dominated fluid) (Zhang et al., 2003; Su et al., 2009a; Wang et al., 2013; Peng et al., 2014; Su et al., 2018). Therefore, the $\delta^{34}S$ values of the fluids are approximately equal to that of the sulfide minerals sedimented from the fluids (Ohmoto, 1972; Ohmoto and Goldhaber, 1997).

The Carlin-type gold deposits in the Youjiang Basin consistently share similar geological characteristics, including the lithology of the host rocks, alteration types, elemental associations, and pyrite textures (Su et al., 2018; Xie et al., 2018a), which suggests that these deposits likely experienced two episodes of hydrothermal processes. Although the $\delta^{34}S$ values of the pyrite cores and rims from most Au deposits in the Youjiang Basin exhibit significant differences, these data were all plotted within two groups (Fig. 12), from approximately −5 to 5‰ and 5 to 15‰. This finding demonstrates that the S isotope compositions of the pyrite cores and rims may have been controlled by similar genetic mechanisms. Gu et al. (2012) revealed a close association between Carlin-type Au mineralization and paleo-oil reservoirs in the Lannigou deposit, thus supporting a coeval model in which the Au originated, migrated, and precipitated simultaneously with hydrocarbon-bearing basin brine systems. The basin brines contain abundant bitumen and organic components, which are also present in the fluid inclusions of the Au deposits in the Youjiang Basin (Zhang et al., 2003; Su et al., 2009a; Wang et al., 2013; Peng et al., 2014; Su et al., 2018). Although no direct S isotopic data were obtained for such brines, Yan et al. (2018) estimated that the basin brines have a $\delta^{34}S$ value of >18‰ based on the highest $\delta^{34}S$ value of Au-bearing pyrite currently reported for the Youjiang Basin (Fig. 12). Consequently, Xie et al. (2018b) and Yan et al. (2018) proposed that the mixing of initial hydrothermal fluids, with $\delta^{34}S$ values of ~0 ± 5‰, and basin brines, with elevated $\delta^{34}S$ values ($\delta^{34}S$ > 18‰), may account for the two groups of S isotope characteristics. Pyrites with lower $\delta^{34}S$ values primarily precipitated from initial hydrothermal fluids while pyrite with higher $\delta^{34}S$ values formed from initial hydrothermal fluids mixed with basin brines.

The initial pre-ore and ore-stage hydrothermal fluids most likely have $\delta^{34}S$ values of ~0 ± 5‰, which may have resulted from a magmatic or deep metamorphic origin (Hou et al., 2016; Xie et al., 2018b; Li et al., 2019; Liang et al., 2020). The Carlin-suite elements are not a common product of fluids derived from deep metamorphic basins. Although As and less Sb are related to fluids sourced from prograde metamorphism, they are generally not associated with Hg (Kesler et al., 2005). Pitcairn et al. (2003) reported that Hg is released during the earliest stage of prograde metamorphism, whereas As and Sb are released at a higher temperature. This decoupling of Hg from As and Sb does not agree with their strong correlation in Carlin-type deposits. Thus, the more likely scenario is a potential magmatic source of S for the original pre-ore and ore-stage fluids.

Despite a scarcity of igneous rocks in the Youjiang Basin from 247 to 95.5 Ma, multiple periods of magmatic activity have been discovered based on accurate geochronological studies. Sparse quartz porphyry dikes (95.5–97 Ma) (Chen et al., 2014; Zhu et al., 2017) have been identified ~10 to 30 km from Au deposits in the northeastern Youjiang Basin (Fig. 1). LA-ICP-MS and SIMS U–Pb dating of inherited zircons from quartz porphyry dikes show age clusters of 130 to 140 and ca. 242 Ma (Zhu et al., 2016), indicating the presence of multiple concealed periods of magmatic activity. Additionally, diabase intrusions (ca. 212–215 Ma) (Pi et al., 2016; Gao, 2018) have been confirmed near Au deposits in the Funing area in the southern Youjiang Basin based on cross-cutting relationships, petrogeochemistry, and geochronology. Together, these data indicate multiple periods of magmatic activity from 247 to 95.5 Ma, which produced multiple periods of hydrothermal events and contributed to the formation of zoned pyrite in the Carlin-type Au deposits in the Youjiang Basin.

6.4. Implications for Au metallogeny

Based on the mineral mapping of the wall rock and ore (Fig. 5), a schematic diagram was drawn to illustrate the two episodes of alteration and mineralization processes in the Lannigou deposit (Fig. 14). Elemental variations across the ore-bearing fault (Fig. 4) indicate that sulfidation, rather than pyritization, accounts for the formation of hydrothermal pyrite in the ore (Hofstra and Cline, 2000; Cline et al., 2005; Su et al., 2009a). The Carlin ore fluid, enriched in reduced S and Au, was principally transported as an Au-HS complex [$Au(HS)^0$ and/or $Au(HS)_2^-$] based on geochemistry experiments (Seward, 1973; Stefánsson and Seward, 2004). The low Au content in Py4 (0.122 ppm), obtained via *in situ* LA-ICP-MS analyses, indicates that the pre-ore hydrothermal fluid was enriched in reduced S, but depleted in Au. During the pre-ore stage, HS^--rich hydrothermal fluid sulfidized Fe primarily via the dissolution of partial siderite and Fe dolomite to produce Py4. Sedimentary pyrite was most likely corroded by the pre-ore hydrothermal activity as no three-layer zoned pyrite was observed in the Lannigou deposit. The relatively high Sb content in Py4, as compared with the sedimentary pyrite (Fig. 8c), implies that the pre-ore hydrothermal fluid was likely characterized by small amounts of Sb. During the ore-forming stage, the $Au(HS)^0$- and/or $Au(HS)_2^-$-rich fluid reacted with residual siderite and Fe dolomite to form OPy. Additionally, the ore fluid reacted with and altered entire albite grains to illite, which fills Py4 or around coarse-grained quartz. The high Au, As, Sb, Tl, Ag, and Cu contents in OPy (Fig. 8) indicate that these elements were the dominating metal elements in the ore-forming fluid.

Quartz veins commonly occur in high-grade ore and contain minor amounts of arsenian pyrite, realgar, stibnite, Fe dolomite, and calcite in the Lanigou deposit (Fig. 3). The sulfides in quartz veins showed an average $\delta^{34}S$ value of 11.6‰, similar to that of OPy, with an average $\delta^{34}S$ value of 12.3‰. Therefore, these quartz veins possibly formed during Au

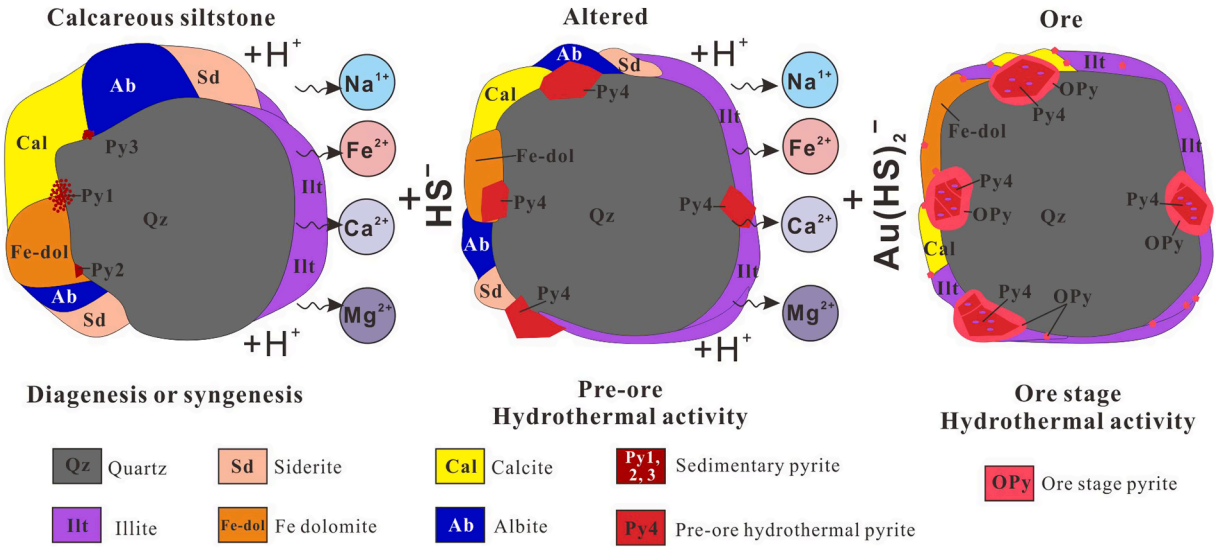

Fig. 14. Schematic diagram showing two episodes of hydrothermal fluids reacting with the host rock (calcareous siltstone), consisting of quartz, illite, calcite, albite, Fe dolomite, siderite, and minor sedimentary pyrite (Py1, Py2, and Py3). At the pre-ore stage, HS^--rich hydrothermal fluid partially sulfidized Fe in siderite and Fe dolomite to form pre-ore hydrothermal pyrite (Py4). At the ore stage, $Au(HS)_2^-$-rich fluid reacted with residual siderite and Fe dolomite to form OPy.

mineralization and were interpreted as ore-stage veins. Zhang et al. (2003) analyzed fluid inclusion in sulfide-bearing quartz veins. The results suggested that the ore fluids were CO_2-rich (7–75 mol. %), low-salinity (<5 wt% NaCl equiv.), and moderately high temperature (240–300 °C) aqueous fluids trapped under pressures of 1.5–2.3 kbar, corresponding to depths of 5.5–8.9 km, assuming lithostatic pressure. However, pre-ore gangue minerals have not been observed or confirmed; refining the physicochemical characteristics of the pre-ore fluid requires additional field observations, geochronology, and isotopic studies.

Schoonen and Barnes (1991) experimentally examined the precipitation of pyrite from solutions between 100 and 300 °C. The rate of direct pyrite nucleation is insignificant in acidic solutions <300 °C, such that pyrite in hydrothermal ore mainly forms via the conversion of a FeS precursor (Schoonen and Barnes, 1991). Owing to the large density of defects or high-energy reactive sites on the surface, newly formed pyrite nuclei can grow rapidly to macroscopic crystals from hydrothermal fluids (Nie et al., 2022). The pre-ore hydrothermal pyrite likely functioned as pyrite nuclei, leading to the rapid crystallization of transported S and the release of Fe from the host rocks during the ore-stage hydrothermal event. Rapid crystallization indicates a non-equilibrium reaction between minerals and fluids; the non-equilibrium partition coefficient is commonly higher than the equilibrium partition coefficient (Xu, 2000). Hence, pre-ore hydrothermal pyrite likely led to the rapid non-equilibrium crystallization of ore-stage pyrite, which then promoted the incorporation of more Au and trace elements into the ore pyrite (Liang et al., 2021).

Although most of the pre-ore hydrothermal pyrite is barren in the Carlin-type Au deposits in the Youjiang Basin, pyrite cores from the Linwang, Gaolong, and Tangshang Au deposits have relatively high Au content, ranging from approximately 1–10 ppm (Fig. 11a) (He et al., 2021; Song et al., 2022; under review). This implies that low-grade Au orebodies may have locally formed during the pre-ore hydrothermal event. Here, we proposed a model involving low-grade Au orebodies formed during the pre-ore hydrothermal event. The ore-stage Au mineralization, superposed with the pre-ore mineralization, may have contributed to the formation of the massive Carlin-type Au deposits.

7. Conclusions

Five distinct pyrite types were identified in the Lannigou deposit: Py1, Py2, Py3, Py4, and OPy. Py1, Py2, and Py3 were primarily discovered in unaltered wall rocks and showed textural and chemical similarities to typical sedimentary pyrite, demonstrating a sedimentary origin. OPy occurred in the rim of coarse pyrite in the ore and contained high Au contents, representing ore-stage hydrothermal pyrite. Py4 occurred in the core of coarse pyrite in the ore, sharing numerous textural and chemical features with typical hydrothermal pyrite, implying an episode of pre-ore hydrothermal alteration. Pre-ore hydrothermal pyrite was also widespread in other Carlin-type Au deposits in the Youjiang Basin. Combining two groups of geochronological data on hydrothermal minerals, we conclude that the Au deposits in the Youjiang Basin most likely experienced two episodes of hydrothermal activity. The pre-ore hydrothermal pyrite likely promoted the rapid non-equilibrium crystallization of ore-stage pyrite, thus facilitating the efficient transfer of Au from the ore fluid to the ore pyrite. Low-grade Au orebodies may have locally formed during the pre-ore hydrothermal event. Multiple hydrothermal events may have been beneficial to the formation of the massive Carlin-type Au deposits in the Youjiang Basin.

Declaration of Competing Interest

The authors declare that they have no known competing financial interests or personal relationships that could have appeared to influence the work reported in this paper.

Acknowledgments

This study was financially supported by grants from the National Natural Science Foundation of China (41803046, U1812402, 41962008, and 42073044) and the Science and Technology Foundation of Guizhou Province (Qiankehezhicheng [2021] YiBan 403, Qiankehejichu [2020] 1Z034, and Qiankehepingtairencai-CXTD [2021] 007). This manuscript benefited from valuable discussions with Dr. Wei Gao. We thank the anonymous reviewers for their constructive comments, which have substantially improved our manuscript. We also thank Xiaolong Wang, Yumin Lu, and Hangxiao Gao for their help with sampling.

Appendix A. Supplementary data

Supplementary data to this article can be found online at https://doi.org/10.1016/j.oregeorev.2022.104816.

References

Aharon, P., Fu, B., 2000. Microbial sulfate reduction rates and sulfur and oxygen isotope fractionations at oil and gas seeps in deepwater Gulf of Mexico. Geochim. Cosmochim. Acta 64 (2), 233–246.

Barker, S.L.L., Hickey, K.A., Cline, J.S., Dipple, G.M., Kilburn, M.R., Vaughan, J.R., Longo, A.A., 2009. Uncloaking invisible gold: Use of nanosims to evaluate gold, trace elements, and sulfur isotope in pyrite from Carlin-type gold. Econ. Geol. 104 (7), 897–904.

Cai, M., He, L., Liu, G., Wu, D., Huang, H., 2006. SHRIMP zircon U-Pb dating of the intrusive rocks in the Dachang tin-polymetallic ore field, Guangxi and their geological significance. Geol. Rev. 52 (3), 409–414 in Chinese with English abstract.

Cail, T.L., Cline, J.S., 2001. Alteration associated with gold deposition at the Getchell Carlin-type gold deposit, north-central Nevada. Econ. Geol. 96 (6), 1343–1359.

Chen, M., Mao, J., Qu, W., Wu, L., Phillip, J.U., 2007. Re-Os dating of arsenian pyrites from the Lannigou gold deposit, Zhenfeng, Guizhou province, and its geological significances. Geol. Rev. 53 (3), 371–382 in Chinese with English abstract.

Chen, M., Huang, Q., Hu, Y., Chen, Z., Zhang, W., 2009. Genetic type of phyllosilicate (micas) and its Ar-Ar dating in Lannigou gold deposit, Guizhou Province, China. Acta Mineral. Sin. 29 (3), 353–362 in Chinese with English abstract.

Chen, M., Mao, J., Bierlein, F.P., Norman, T., Uttley, P.J., 2011. Structural features and metallogenesis of the Carlin-type Jinfeng (Lannigou) gold deposit, Guizhou Province, China. Ore Geol. Rev. 43 (1), 217–234.

Chen, M., Lu, G., Li, X., 2012. Muscovite 40Ar/39Ar dating of the quartz porphyry veins from northwest Guangxi, China, and its geological significance. Geol. J. China Univ. 18 (1), 106–116 in Chinese wiht English abstract.

Chen, M., Zhang, Y., Meng, Y., Lu, G., Liu, S., 2014. Determination of upper limit of metallogenic epoch of Liaotun gold deposit in western Guangxi and its implications for chronology of Carlin-type gold deposits in Yunnan-Guizhou-Gangxi golden triangle area. Mineral Deposits 33, 1–13 in Chinese with English abstract.

Chen, M., Mao, J., Li, C., Zhang, Z., Dang, Y., 2015. Re–Os isochron ages for arsenopyrite from Carlin-like gold deposits in the Yunnan–Guizhou–Guangxi “golden triangle”, southwestern China. Ore Geol. Rev. 64, 316–327.

Chen, M., Bagas, L., Liao, X., Zhang, Z., Li, Q., 2019. Hydrothermal apatite SIMS Th-Pb dating: Constraints on the timing of low-temperature hydrothermal Au deposits in Nibao, SW China. Lithos 324–325, 418–428.

Cheng, Y., Mao, J., 2010. Age and geochemistry of granites in Gejiu area, Yunnan province, SW China: constraints on their petrogenesis and tectonic setting. Lithos 120 (3), 258–276.

Cheng, Y., Mao, J., Chen, X., Li, W., 2010. LA-ICP-MS zircon U-Pb dating of the Bozhushan granite in Southeastern Yunnan Province and its significance. J. Jilin Univ. Earth Sci. Ed. 40 (4), 869–878 in Chinese with English abstract.

Clark Maroun, L.R., Cline, J.S., Simon, A., Anderson, P., Muntean, J., 2017. High-grade gold deposition and collapse breccia formation, Cortez Hills Carlin-type gold deposit, Nevada, USA. Econ. Geol. 112 (4), 707–740.

Cline, J.S., Hofstra, A.H., Muntean, J.L., Tosdal, R.M., Hickey, K.A., 2005. Carlin-type gold deposits in Nevada: Critical geologic characteristics and viable models. In: Hedenquist, J.W., Thompson, J.F.H., Goldfarb, R.J., Richards, J.P. (Eds.), Economic Geology 100th anniversary volume. Society of Economic Geologists Inc, Littleton, pp. 451–484.

Cline, J.S., Muntean, J.L., Gu, X., Xia, Y., 2013. A comparison of Carlin-type gold deposits: Guizhou Province, golden triangle, southwest China, and northern Nevada, USA. Earth Sci. Front. 20 (1), 1–18.

Dong, W., 2017. Geochemistry of diabase-hosted gold deposit along the southern margin of Youjiang basin. Ph.D. Thesis, University of Chinese Academy of Sciences, Beijing, China (in Chinese with English abstract).

Du, Y., Huang, H., Yang, J., Huang, H., Tao, P., Huang, Z., Hu, L., Xie, C., 2013. The basin translation from late Paleozoic to Triassic of the Youjiang basin and its tectonic signification. Geol. Rev. 59 (1), 1–11 in Chinese with English abstract.

Emsbo, P., Hofstra, A.H., Lauha, E.A., Griffin, G.L., Hutchinson, R.W., 2003. Origin of high-grade gold ore, source of ore fluid components, and genesis of the Meikle and Neighboring Carlin-Type deposits, Northern Carlin Trend, Nevada. Econ. Geol. 98 (6), 1069–1105.

Frimmel, H.E., 2008. Earth’s continental crustal gold endowment. Earth Planet. Sci. Lett. 267 (1–2), 45–55.

Gao, W., 2018. Geochronology and Dynamics of Carlin-type gold deposits in the Youjiang basin (NW Guangxi). Ph.D. Thesis, University of Chinese Academy of Sciences, Beijing, China (in Chinese with English abstract).

Gao, W., Hu, R., Hofstra, A.H., Li, Q., Zhu, J., Peng, K., Mu, L., Huang, Y., Ma, J., Zhao, Q., 2021. U-Pb dating on hydrothermal rutile and monazite from the Badu gold deposit supports an Early Cretaceous age for Carlin-type gold mineralization in the Youjiang Basin, Southwestern China. Econ. Geol. 116(6), 1355-1385.

Ge, X., Selby, D., Liu, J., Chen, Y., Cheng, G., Shen, C., 2021. Genetic relationship between hydrocarbon system evolution and Carlin-type gold mineralization: Insights from Re-Os pyrobitumen and pyrite geochronology in the Nanpanjiang Basin, South China. Chem. Geol. 559, 119953.

Gregory, D.D., Large, R.R., Halpin, J.A., Baturina, E.L., Lyons, T.W., Wu, S., Danyushevsky, L., Sack, P.J., Chappaz, A., Maslennikov, V.V., Bull, S.W., 2015. Trace element content of sedimentary pyrite in black shales. Econ. Geol. 110 (6), 1389–1410.

Groves, D.I., Goldfarb, R.J., Gebre-Mariam, M., Hagemann, S.G., Robert, F., 1998. Orogenic gold deposits: a proposed classification in the context of their crustal distribution and relationship to other gold deposit types. Ore Geol. Rev. 13 (1), 7–27.

Gu, X., Zhang, Y., Li, B., Dong, S., Xue, C., Fu, S., 2012. Hydrocarbon- and ore-bearing basinal fluids: A possible link between gold mineralization and hydrocarbon accumulation in the Youjiang basin, South China. Miner. Deposita 47 (6), 663–682.

He, X., Su, W., Shen, N., Xia, X., Wang, F., 2021. In situ multiple sulfur isotopes and trace element compositions of pyrite support a sedimentary source-rock model for Linwang Carlin-type gold deposit in the Youjiang basin, Southwest China. Ore Geol. Rev. 139, 104533.

Hofstra, A.H., Cline, J.S., 2000. Characteristics and models for Carlin-type gold deposits. Rev. Econ. Geol. 13, 163–220.

Hou, L., Peng, H., Ding, J., Zhang, J., Zhu, S.B., Wu, S., Wu, Y., Ouyang, H., 2016. Textures and in situ chemical and isotopic analyses of pyrite, Huijiabao trend, Youjiang Basin, China: implications for paragenesis andsource of sulfur. Econ. Geol. 111 (2), 331–353.

Hu, R., Su, W., Bi, X., Tu, G., Hofstra, A.H., 2002. Geology and geochemistry of Carlin-type gold deposits in China. Miner. Deposita 37, 378–392.

Hu, R., Fu, S., Huang, Y., Zhou, M., Fu, S., Zhao, C., Wang, Y., Bi, X., Xiao, J., 2017. The giant South China Mesozoic low-temperature metallogenic domain: reviews and a new geodynamic model. J. Asian Earth Sci. 137, 9–34.

Hu, X., Zeng, G., Zhang, Z., Li, W., Liu, W., Gong, Y., Yao, S., 2018. Gold mineralization associated with Emeishan basaltic rocks: mineralogical, geochemical, and isotopic evidences from the Lianhuashan ore field, southwestern Guizhou Province, China. Ore Geol. Rev. 95, 604–619.

Huang, Y., Hu, R., Bi, X., Fu, S., Peng, K., Gao, W., Oyebamiji, A., Zhaanbaeva, A., 2019. Low-temperature thermochronology of the Carlin-type gold deposits in southwestern Guizhou, China: implications for mineralization age and geological thermal events. Ore Geol. Rev. 115, 103178.

Ilchik, R.P., Barton, M.D., 1997. An amagmatic origin of Carlin-type gold deposits. Econ. Geol. Bull. Soc. Econ. Geol. 92 (3), 269–288.

Ilchik, R.P., Uttley, P.J., Corben, R., Zhang, A.Y., Ham, A.P., Hodkiewicz, P., 2005. The Jinfeng gold deposit: Mining the new frontier of China. In: Rhoden, H.N., Steininger, R.C., Vikre, P.G. (Eds.), Window to the world: 2005 Symposium proceedings. Reno, Nevada, Geological Society of, Nevada, pp. 887–898.

Jiang, W., Xiang, Z., Xia, W., Xia, L., Zhang, H., Pham, V.T., Yan, Q., Wei, W., 2017. Are the mafic intrusive rocks in the Funing area, Southeast Yunnan (Southwest China), really derived from the Emeishan plume? New evidence from geological surveys of the Dongbo and Guichao sheets (1:50000). Acta Petrol. Sin. 33 (10), 3109–3122 in Chinese with English abstract.

Jin, X., 2017. Geology, mineralization and genesis of the Nibao, Shuiyindong and Yata gold deposits in SW Guizhou Province, China. Ph.D. Thesis, China University of Geosciences, Wuhan, China (in Chinese with English abstract).

Jin, X., Zhao, J., Feng, Y., Hofstra, A.H., Deng, X., Zhao, X., Li, J., 2021. Calcite U-Pb dating unravels the age and hydrothermal history of the giant Shuiyindong Carlin-type gold deposit in the golden triangle, South, China. Econ. Geol. 116 (6), 1253–1265.

Kesler, S.E., Riciputi, L.C., Ye, Z., 2005. Evidence for a magmatic origin for Carlin-type gold deposits: Isotopic composition of sulfur in the Betze-Post-Screamer deposit, Nevada, USA. Miner. Deposita 40 (2), 127–136.

Lai, C.-K., Meffre, S., Crawford, A.J., Zaw, K., Xue, C.-D., Halpin, J.A., 2014. The western ailaoshan volcanic belts and their SE asia connection: a new tectonic model for the Eastern Indochina Block. Gondwana Res. 26 (1), 52–74.

Large, R.R., Halpin, J.A., Danyushevsky, L.V., Maslennikov, V.V., Bull, S.W., Long, J.A., Gregory, D.D., Lounejeva, E., Lyons, T.W., Sack, P.J., McGoldrick, P.J., Calver, C.R., 2014. Trace element content of sedimentary pyrite as a new proxy for deep-time ocean–atmosphere evolution. Earth Planet. Sci. Lett. 389, 209–220.

Li, J., 2019. Study on the metallogenetic source and the fluid evolution of Carlin type gold deposits-a case study of in situ sulfur isotopes and trace elements of pyrites of gold deposits from two sedimentary facies in the Youjiang Basin. Ph.D. Thesis, University of Chinese Academy of Sciences, Beijing, China (in Chinese with English abstract).

Li, J., Zhao, C., Huang, Y., Zhuo, Y., Li, J., 2019. In-situ sulfur isotope and trace element of pyrite constraints on the formation and evolution of the Nibao Carlin-type gold deposit in SW China. Acta Geochimica, 38(4), 555-575.

Li, J., Hu, R., Zhao, C., Zhu, J., Huang, Y., Gao, W., Li, J., Zhuo, Y., 2020. Sulfur isotope and trace element compositions of pyrite determined by NanoSIMS and LA-ICP-MS: new constraints on the genesis of the Shuiyindong Carlin-like gold deposit in SW China. Miner. Deposita 55 (7), 1279–1298.

Li, Z., Li, X., 2007. Formation of the 1300-km-wide intracontinental orogen and postorogenic magmatic province in Mesozoic South China: a flat-slab subduction model. Geology 35 (2), 179–182.

Liang, J., Li, J., Liu, X., Zhai, W., Huang, Y., Zhao, J., Sun, W., Song, M., Li, J., 2020. Multiple element mapping and in-situ S isotopes of Au-carrying pyrite of Shuiyindong gold deposit, southwestern China using NanoSIMS: Constraints on Au sources, ore fluids, and mineralization processes. Ore Geol. Rev. 123, 103576.

Liang, Q., Xie, Z., Song, X., Wirth, R., Xia, Y., Cline, J., 2021. Evolution of invisible Au in arsenian pryite in Carlin-type Au deposits. Econ. Geol. 116 (2), 515–526.

Lin, S., Hu, K., Cao, J., Bai, T., Liu, Y., Han, S., 2021. An in situ sulfur isotopic investigation of the origin of Carlin-type gold deposits in Youjiang Basin, southwest China. Ore Geol. Rev. 134, 104187.

Liu, J., Wang, Z., Yang, C., Li, J., Xie, Z., Zheng, L., Tan, Q., Song, W., Xu, L., Li, S., Wang, D., Chen, F., Qin, Y., Tan, L., Hu, C., 2020. Multi-level structural detachment mineralization system of Carlin-type gold deposits in southern China. China Sci. Technol. Achievements 21 (14), 49–51 in Chinese with English abstract.

Liu, P., Li, P., Ma, R., Han, Z., Yang, G., Ye, D., 2006. A gold deposit associated with pyroclastic rock and hydrothermal exhalation: Nibao gold deposit in Guizhou Province, China. Mineral Deposits 25 (1), 101–110 in Chinese with English abstract.

Liu, S., Su, W., Hu, R., Feng, C., Gao, S., Coulson, I.M., Wang, T., Feng, G., Tao, Y., Xia, Y., 2010. Geochronological and geochemical constraints on the petrogenesis of alkaline ultramafic dykes from southwest Guizhou Province, SW China. Lithos 114 (1), 253–264.

Liu, Y., Li, Z., Li, H., Guo, L., Xu, W., Ye, L., Li, C., Pi, D., 2007. U-Pb geochronology of cassiterite and zircon from the Dulong Sn-Zn deposit: Evidence for Cretaceous large-scale granitic magmatism and mineralization events in southeastern Yunnan province, China. Acta Petrol. Sin. 23 (5), 967–976 in Chinese with English abstract.
Mao, J., Cheng, Y., Chen, M., Franco, P., 2013. Major types and time–space distribution of Mesozoic ore deposits in South China and their geodynamic settings. Miner. Deposita 48 (3), 267–294.
Muntean, J.L., Cline, J.S., Simon, A.C., Longo, A.A., 2011. Magmatic-hydrothermal origin of Nevada's Carlin-type gold deposits. Nat. Geosci. 4 (2), 122–127.
Muntean, J.L., Cline, J.S., 2018. Introduction diversity of Carlin-style gold deposits. In: Muntean, J.L. (Ed.), Diversity of Carlin-style gold deposits, Reviews in Economic Geology. Society of Economic Geologists Inc, Colorado, USA, pp. 1–5.
Nie, X., Li, G., Wang, Y., Luo, Y., Song, L., Yang, S., Wan, Q., 2022. Highly efficient removal of Cr(VI) by hexapod-like pyrite nanosheet clusters. J. Hazard. Mater. 424, 127504.
Ohmoto, H., 1972. Systematics of sulfur and carbon isotopes in hydrothermal ore deposits. Econ. Geol. 67 (5), 551–578.
Ohmoto, H., Goldhaber, M.B., 1997. Sulfur and Carbon Isotopes. John Wiley & Sons, New York.
Peng, Y., Gu, X., Zhang, Y., Liu, L., Wu, C., Chen, S., 2014. Ore-forming process of the Huijiabao gold district, southwestern Guizhou Province, China: evidence from fluid inclusions and stable isotopes. J. Asian Earth Sci. 93, 89–101.
Pi, Q., Hu, R., Peng, K., Wu, J., Wei, Z., Huang, Y., 2016. Geochronology of the Zhesang gold deposit and mafic rock in Funing County of Yunnan Province, with special reference to the dynamic background of Carlin-type gold deposits in the Dian-Qian-Gui region. Acta Petrol. Sin. 32 (11), 3331–3342 in Chinese with English abstract.
Pi, Q., Hu, R., Xiong, B., Li, Q., Zhong, R., 2017. In situ SIMS U-Pb dating of hydrothermal rutile: reliable age for the Zhesang Carlin-type gold deposit in the golden triangle region, SW China. Miner. Deposita 52 (8), 1179–1190.
Pitcairn, I.K., Ashley, M.R., Teagle, D.A.H., Green, D.R.H., German, C.R., Croudace, I.W., Brewer, T.S., Craw, D., 2003. Mobility of Hg, As, Sb, S and C in a metamorphic belt: insights into the source of elements enriched in orogenic gold deposits, the Otago Schists, New Zealand. In: Millpress, D.G.E. (Ed.), Mineral exploration and sustainable development. Rotterdam, pp. 803–806.
Ressel, M.W., Henry, C.D., 2006. Igneous geology of the Carlin trend, Nevada: development of the eocene plutonic complex and significance for Carlin-type gold deposits. Econ. Geol. 101 (2), 347–383.
Schoonen, M.A.A., Barnes, H.L., 1991. Mechanisms of pyrite and marcasite formation from solution: III. Hydrothermal processes. Geochim. Cosmochim. Acta 55 (12), 3491–3504.
Seward, T.M., 1973. Thio-complexes of gold in hydrothermal ore solutions. Geochim. Cosmochim. Acta 37, 379–399.
Shen, Y., Buick, R., Canfield, D.E., 2001. Isotopic evidence for microbial sulphate reduction in the early Archaean era. Nature 410 (6824), 77–81.
Song, W., Wu, P., Liu, J., Li, J., Wang, Z., Chen, F., Tan, Q., Xie, Z. Under Review. Genesis of the Carlin-type gold deposits in Youjiang basin, Southwestern China: a case study of basalt-hosted Tangshang gold deposit. J. Earth Sci.
Song, W., Wu, P., Liu, J., Li, J., Wang, Z., Tan, Q., Xie, Z., 2022. Genesis of the Gaolong gold deposit in Northwest Guangxi Province, South China: insights from in situ trace elements and sulfur isotopes of pyrite. Ore Geol. Rev. 104782.
Su, W., Heinrich, C.A., Pettke, T., Zhang, X., Hu, R., Xia, B., 2009a. Sediment-hosted gold deposits in Guizhou, China: products of wall-rock sulfidation by deep crustal fluids. Econ. Geol. 104 (1), 73–93.
Su, W., Hu, R., Xia, B., Xia, Y., Liu, Y., 2009b. Calcite Sm-Nd isochron age of the Shuiyindong Carlin-type gold deposit, Guizhou, China. Chem. Geol. 258 (3), 269–274.
Su, W., Zhang, H., Hu, R., Ge, X., Xia, B., Chen, Y., Zhu, C., 2012. Mineralogy and geochemistry of gold-bearing arsenian pyrite from the Shuiyindong Carlin-type gold deposit, Guizhou, China: implications for gold depositional processes. Miner. Deposita 47 (6), 653–662.
Su, W., Dong, W., Zhang, X., Shen, N., Hu, R., Hofstra, A.H., Cheng, L., Xia, Y., Yang, K., 2018. Carlin-type gold deposits in the Dian-Qian-Gui "golden triangle" of Southwest China. In: Muntean, J.L. (Ed.), Diversity of Carlin-Style Gold Deposits, Reviews in Economic Geology. Society of Economic Geologists Inc, Colorado, USA, pp. 157–185.
Stefánsson, A., Seward, T.M., 2004. Gold(I) complexing in aqueous sulphide solutions to 500°C at 500 bar. Geochim. Cosmochim. Acta 68, 4121–4143.
Tan, Q., Xia, Y., Xie, Z., Yan, J., 2015. Migration paths and precipitation mechanisms of ore-forming fluids at the Shuiyindong Carlin-type gold deposit, Guizhou, China. Ore Geol. Rev. 69, 140–156.
Tan, Q., Xia, Y., Xie, Z., Wang, Z., Wei, D., Zhao, Y., Yan, J., Li, S., 2019. Two hydrothermal events at the Shuiyindong Carlin-Type gold deposit in Southwestern China: insight from Sm–Nd dating of fluorite and calcite. Minerals 9 (4), 230.
Wang, Z., Xia, Y., Song, X., Liu, J., Yang, C., Yan, B., 2013. Study on the evolution of ore-formation fluids for Au-Sb ore deposits and the mechanism of Au-Sb paragenesis and differentiation in the southwestern part of Guizhou Province, China. Chin. J. Geochem. 32 (1), 56–68.
Wang, Z., Tan, Q., Xia, Y., Liu, J., Yang, C., Li, S., Li, J., Chen, F., Wang, X., Pan, Q., Wang, D., 2021. Sm–Nd isochron age constraints of Au and Sb mineralization in Southwestern Guizhou Province, China. Minerals 11 (2), 100.
Wei, D., Xia, Y., Gregory, D.D., Steadman, J.A., Tan, Q., Xie, Z., Liu, X., 2020. Multistage pyrites in the Nibao disseminated gold deposit, southwestern Guizhou Province, China: insights into the origin of Au from textures, in situ trace elements, and sulfur isotope analyses. Ore Geol. Rev. 122, 103446.
Xie, Z., Xia, Y., Cline, J.S., Koenig, A., Wei, D., Tan, Q., Wang, Z., 2018a. Are there Carlin-type gold deposits in China? a comparison of the Guizhou, China, deposits with Nevada, USA, deposits. In: Muntean, J.L. (Ed.), Diversity of Carlin-Style Gold Deposits, Reviews in Economic Geology. Society of Economic Geologists Inc, Colorado, USA, pp. 187–233.
Xie, Z., Xia, Y., Cline, J.S., Pribil, M.J., Koenig, A., Tan, Q., Wei, D., Wang, Z., Yan, J., 2018b. Magmatic origin for sediment-hosted Au deposits, Guizhou Province, China: in situ chemistry and sulfur isotope composition of pyrites, Shuiyindong and Jinfeng deposits. Econ. Geol. 113 (7), 1627–1652.
Xu, H., 2000. Investigation of invisible Au in Au-bearing FeS2 microcrystals from Carlin gold ore deposit, Nevada, USA: TEM study and geochemical modeling. Geol. J. China Univ. 6 (4), 532–545.
Yan, J., Hu, R., Liu, S., Lin, Y., Zhang, J., Fu, S., 2018. NanoSIMS element mapping and sulfur isotope analysis of Au-bearing pyrite from Lannigou Carlin-type Au deposit in SW China: new insights into the origin and evolution of Au-bearing fluids. Ore Geol. Rev. 92, 29–41.
Zaw, K., Meffre, S., Lai, C.-K., Burrett, C., Santosh, M., Graham, I., Manaka, T., Salam, A., Kamvong, T., Cromie, P., 2014. Tectonics and metallogeny of mainland Southeast Asia — A review and contribution. Gondwana Res. 26 (1), 5–30.
Zhang, X., Spiro, B., Halls, C., Stanley, C.J., Yang, K., 2003. Sediment-hosted disseminated gold deposits in Southwest Guizhou, PRC: their geological setting and origin in relation to mineralogical, fluid inclusion, and stable-isotope characteristics. Int. Geol. Rev. 45 (5), 407–470.
Zhao, C., 2014. Sulfide mineralogy and genetic model of the Lannigou Carlin-type gold deposit in Southwestern Guizhou, China. Ph.D. Thesis, University of Chinese Academy of Sciences, Beijing, China (in Chinese with English abstract).
Zhao, J., Liang, J., Li, J., Ni, S., Xiang, Q., Nan, Z., 2019. Mineralogical characteristics and in situ sulfur isotopic compositions of Au-bearing pyrites in the Taipingdong gold deposit, Guizhou Province. Geotectonica et Metallogenia, 43(2), 258-270 (in Chinese with English abstract).
Zhao, J., Liang, J., Li, J., Huang, Y., Liu, X., Zhang, J., Hao, J., Sun, W., Li, J., Xie, J., 2020. Gold and sulfur sources of the Taipingdong Carlin-type gold deposit: Constraints from simultaneous determination of sulfur isotopes and trace elements in pyrite using nanoscale secondary ion mass spectroscopy. Ore Geol. Rev. 117, 103299.
Zhao, Z., Hou, L., Ding, J., Zhang, Q., Wu, S., 2018. A genetic link between Late Cretaceous granitic magmatism and Sn mineralization in the southwestern South China Block: a case study of the Dulong Sn-dominant polymetallic deposit. Ore Geol. Rev. 93, 268–289.
Zheng, L., Yang, R., Gao, J., Chen, J., Liu, J., Li, D., 2019. Quartz Rb-Sr isochron ages of two type orebodies from the Nibao Carlin-Type gold deposit, Guizhou, China. Minerals 9 (7), 1–15.
Zhou, M., Zhao, J., Qi, L., Su, W., Hu, R., 2006. Zircon U-Pb geochronology and elemental and Sr–Nd isotope geochemistry of Permian mafic rocks in the Funing area, SW China. Contrib. Miner. Petrol. 151 (1), 1–19.
Zhu, J., Zhong, H., Xie, G., Zhao, C., Xu, L., Lu, G., 2016. Origin and geological implication of the inherited zircon from felsic dykes. Acta Petrol. Sin. 32 (11), 3260–3280 in Chinese with English abstract.
Zhu, J., Hu, R., Richards, J.P., Bi, X., Stern, R., Lu, G., 2017. No genetic link between Late Cretaceous felsic dikes and Carlin-type Au deposits in the Youjiang basin, Southwest China. Ore Geol. Rev. 84, 328–337.